Selection of independent components based on cortical mapping of electromagnetic activity

2012 J. Neural Eng. 9 056006

(http://iopscience.iop.org/1741-2552/9/5/056006)

J. Neural Eng. **9** (2012) 056006 (18pp) doi:10.1088/1741-2560/9/5/056006

Selection of independent components based on cortical mapping of electromagnetic activity

Hui-Ling Chan[1], **Yong-Sheng Chen**[1,4] **and Li-Fen Chen**[2,3]

[1] Department of Computer Science, National Chiao Tung University, Hsinchu, Taiwan
[2] Institute of Brain Science, National Yang-Ming University, Taipei, Taiwan
[3] Department of Medical Research and Education, Taipei Veterans General Hospital, Taipei, Taiwan

E-mail: hlchan@cs.nctu.edu.tw, yschen@cs.nctu.edu.tw and lfchen@ym.edu.tw

Received 6 March 2012
Accepted for publication 4 July 2012
Published 10 August 2012
Online at stacks.iop.org/JNE/9/056006

Abstract
Independent component analysis (ICA) has been widely used to attenuate interference caused by noise components from the electromagnetic recordings of brain activity. However, the scalp topographies and associated temporal waveforms provided by ICA may be insufficient to distinguish functional components from artifactual ones. In this work, we proposed two component selection methods, both of which first estimate the cortical distribution of the brain activity for each component, and then determine the functional components based on the parcellation of brain activity mapped onto the cortical surface. Among all independent components, the first method can identify the dominant components, which have strong activity in the selected dominant brain regions, whereas the second method can identify those inter-regional associating components, which have similar component spectra between a pair of regions. For a targeted region, its component spectrum enumerates the amplitudes of its parceled brain activity across all components. The selected functional components can be remixed to reconstruct the focused electromagnetic signals for further analysis, such as source estimation. Moreover, the inter-regional associating components can be used to estimate the functional brain network. The accuracy of the cortical activation estimation was evaluated on the data from simulation studies, whereas the usefulness and feasibility of the component selection methods were demonstrated on the magnetoencephalography data recorded from a gender discrimination study.

(Some figures may appear in colour only in the online journal)

1. Introduction

Independent component analysis (ICA) is a type of blind source separation method, capable of decomposing mixed signals into mutually independent components (ICs) (Bell and Sejnowski 1995, Comon 1994). It has been widely used to disentangle magnetoencephalographic (MEG) and electroencephalographic (EEG) signals, particularly to attenuate interference caused by noise through the removal of artifactual components from the acquired data (Cao *et al* 2003, Dammers *et al* 2008, Delorme *et al* 2007, Escudero *et al* 2007, Fatourechi *et al* 2007, Joyce *et al* 2004, Jung *et al* 2000, Lemm *et al* 2006, Li *et al* 2006, Lu *et al* 2012, Mantini *et al* 2008, Rong and Contreras-Vidal 2006). This preprocessing step can increase the accuracy of spike detection in single-trial recordings (De Lucia *et al* 2008, Ossadtchi *et al* 2004), the identification of the neuronal event-related potential (Lee *et al* 2003, Pritchard *et al* 1999, Saatchi 2004, Tang *et al* 2002a, Turi *et al* 2012, Vigário *et al* 2000), the classification of neural activity in brain–computer interface systems (Kachenoura *et al* 2008, Kamousi *et al* 2007, Lee *et al* 2006, Lou *et al* 2008, Serby *et al* 2005, Xu *et al* 2004) and source localization (Debener

[4] Author to whom any correspondence should be addressed.

et al 2007, Kobayashi *et al* 2002, Mantini *et al* 2008, Tang *et al* 2002b, Zhukov *et al* 2000).

Following component decomposition, the next step involves distinguishing the functional ICs from the artifactual ones, according to their temporal waveforms and scalp topographies, which are spatial distributions of electric potentials/magnetic fields mapped on/over the scalp surface, respectively. However, the electromagnetic recordings originating from a single source of brain activity may be decomposed into several ICs, particularly when many channels are engaged (Makeig *et al* 1999, Viola *et al* 2009). In this case, it is difficult to individually determine whether an IC is a functional component according to the scattered information in its temporal waveform and scalp topography. One possible way to avoid this over-splitting problem is to estimate the model order of ICA decomposition (Roberts and Everson 2000). On the other hand, different source distributions may result in similar scalp topographies (Fogelson *et al* 2004). Therefore, selection of functional ICs should comprehensively consider the holistic information of the cortical source distributions estimated from all ICs.

The source information of an IC can be calculated by estimating the associated brain activity from the scalp topography of the IC. Dipole fitting (Scherg and Von Cramon 1985) is a widely used method for source localization (Cao *et al* 2002, Debener *et al* 2005, Makeig *et al* 2004, Onton *et al* 2005, Sercheli *et al* 2009). However, this method requires a fixed number of dipoles and initial guesses of dipole parameters to be made in advance (Michel *et al* 2004). The simple assumption that there is only one dipole source associated with every IC (Cao *et al* 2002, Latif *et al* 2007, Zhukov *et al* 2000) is generally not true, particularly when an IC is associated with synchronized activity among multiple regions of the brain (Tang *et al* 2005). Furthermore, it has been reported that estimation results are heavily influenced by the initial guesses regarding the parameters in the dipole source model (Cuffin 1998, Grech *et al* 2008).

Electromagnetic spatiotemporal independent component analysis (EMSICA) (Tsai *et al* 2006) is another way to calculate the source information for each IC. The conventional ICA method is modified to simultaneously estimate the independent temporal dynamics and their corresponding cortical activation topographies. This method utilizes the Bayesian statistical framework for imaging independent brain activity using implicit and explicit constraints. Compared to the temporal ICs obtained by the conventional ICA method, EMSICA estimates the spatiotemporal ICs at the expense of other unknown parameters, and thus may increase the risk of instability in the estimation of the unmixing matrix.

This paper first presents an approach to cortical mapping that estimates a cortical activation topography from the scalp MEG/EEG topography for each IC. Moreover, we propose two component selection methods to determine functional components based on the estimated cortical source distribution. Instead of the assumption of spatial independence imposed in EMSICA, our approach uses conventional ICA to decompose the MEG/EEG measurements, whereupon the cortical activation topography is estimated with a minimum norm constraint. Component decomposition using conventional ICA is more stable and efficient than EMSICA because it requires fewer unknown parameters. Furthermore, using the proposed cortical mapping approach to estimate the cortical activation topography is more flexible because different kinds of ICA methods can be used to decompose MEG/EEG signals according to their characteristics (Kachenoura *et al* 2008).

Based on the spatial and temporal information of each IC, a variety of procedures has been proposed for the determination of functional components, such as visual inspection, template-based approaches, and clustering analysis methods. Visual inspection is the most commonly used method for classifying functional ICs and non-functional artifacts (Debener *et al* 2005, 2008, Fogelson *et al* 2004, Jung *et al* 2000). However, the selection results tend to be inconsistent and subjective (Naeem *et al* 2006). Template-based approaches are capable of automatically identifying ICs with characteristics similar to those of the spatial or temporal templates provided beforehand (De Martino *et al* 2007, Lee *et al* 2003, Wessel and Ullsperger 2011). Although the results are more consistent than those obtained from visual inspection, the criteria for the construction of templates may bias the selection results.

The idea behind clustering-based approaches (Contreras-Vidal and Kerick 2004, Himberg *et al* 2004, Jervis *et al* 2007, Jung *et al* 2001, Milanesi *et al* 2009, Onton *et al* 2005) is to categorize ICs into several groups, such that the within-group spatiotemporal characteristics are similar but the between-group ones are dissimilar. Although there is no need for prior knowledge regarding the spatiotemporal characteristics of function-related activity, the clustering results are sensitive to the type of features, clustering methods, and the associated parameters. These approaches essentially focus on the statistical characteristics of ICs but not on their physiological interpretation. Furthermore, clustering approaches are inherently time-consuming, particularly when the datasets are diverse or the number of features is large (Viola *et al* 2009). Moreover, these approaches often encounter difficulties associated with inter-participant variation, the multiple executions of ICA, and the large number of ICs (Groppe *et al* 2009). By combining template-based and clustering-based methods, a hybrid algorithm, CORRMAP (Viola *et al* 2009), has been proposed to identify a compact cluster of ICs similar to a specific spatial template.

This paper proposes two component selection methods that utilize the parceled cortical activity of all components to provide statistical guidance for the selection of two categories of functional components. The first category includes the dominant components, which are highly active in dominant regions. The second category includes inter-regional associating components with similar component spectra for a pair of regions in the brain. The component spectrum of a region enumerates the amplitudes of the cortical activity across all components. To complete a task, several networks in the brain work together and a single region of the brain may be involved in different networks. The regions of a brain network communicate with each other through synchronized brain activity (Engdahl *et al* 2010, Georgopoulos *et al* 2007, 2010,

Varela *et al* 2001). The cortical source distribution of an IC contains vertices that have the same temporal activation pattern as the temporal waveform of the IC. Thus, the distribution may represent one functional brain network because regions with high amplitudes apparently reveal the synchronized brain activity. The conventional approaches for estimating the connectivity of brain networks consider the relationship between the brain activity of different regions. However, brain activity in one region may include activity that does not belong to the networks involving the pair of regions. The proposed associating component selection method quantifies network connectivity by considering the contribution of activity to the network. Moreover, the proposed selection methods are based on anatomical structure, making them more objective than visual inspection and the template-based methods. Compared to the clustering-based method, our methods not only consider the features extracted from statistical analysis but also allow users to specify regions of interest based on their prior knowledge.

The proposed algorithms for estimating the cortical activation topographies of ICs and selecting functional components are described in section 2. In section 3, we present the evaluation results pertaining to the accuracy and feasibility of the proposed algorithms using five sets of simulation data as well as the data from a gender discrimination study. The advantages and limitations of the proposed algorithms are addressed in section 4. Conclusions are drawn in section 5.

2. Materials and methods

This section describes the proposed methods of component selection for MEG signal analysis. First, the cortical activation topography is estimated for each IC. The estimation method consists of a forward model, which represents the relationship between sources of brain activity and MEG measurements, a general linear model, which relates the cortical activation topography to the scalp topography, and the minimum norm solution to this linear model. Based on the estimated cortical activation topographies, the proposed component selection algorithms are capable of determining both dominant components with a high degree of activity in the specified regions and inter-regional associating components, which have similar component spectra and high cumulative activity in a pair of regions. Note that the proposed methods can also be applied to the analysis of EEG signals.

2.1. Forward model

In the MEG forward model, the lead field vector $\mathbf{l}_\theta \in \Re^C$ indicates how the unit dipole with parameters $\boldsymbol{\theta} = \{\mathbf{r}, \mathbf{q}\}$ contributes to the measurements of the MEG sensor array:

$$\mathbf{l}_\theta = \mathbf{G}_\mathbf{r}\mathbf{q}, \tag{1}$$

where $\mathbf{G}_\mathbf{r} \in \Re^{C\times 3}$ is the gain matrix describing the sensitivity of C MEG sensors to the current dipole source located at $\mathbf{r} \in \Re^3$ and $\mathbf{q} \in \Re^3$ is a unit vector representing the dipole orientation (Baillet *et al* 2001, Mosher *et al* 1999, Sekihara and Nagarajan 2008).

MEG measurements are induced by an ensemble of neuronal activity throughout the entire brain, which can be represented by a distributed source model. Assume that there are P vertices on the cortical surface and each vertex is associated with a dipole with parameters $\boldsymbol{\theta}_p = \{\mathbf{r}_p, \mathbf{q}_p\}$, $p = 1, 2, \ldots, P$, where $\mathbf{r}_p$ is the vertex position and $\mathbf{q}_p$ is the orientation of the dipole located at $\mathbf{r}_p$. There are two ways to determine the dipole orientation $\mathbf{q}_p$. The first is the surface-constrained method, which assumes that the dipole is aligned with the normal direction of the cortical surface. This type of anatomical information can be obtained through cortex segmentation of magnetic resonance (MR) images. The other method is a data-driven approach, which estimates the dipole orientation solely from MEG measurements. For example, the maximum contrast beamformer (MCB) provides an analytical solution to the dipole orientation subject to a minimum variance and maximum contrast criterion as well as unit-gain constraint (Chen *et al* 2006).

The measurements $\mathbf{m}(t) = [m_1(t)\ m_2(t)\ \ldots\ m_C(t)]^T \in \Re^C$ and dipole activity $\mathbf{s}(t) = [s_1(t)\ s_2(t)\ \ldots\ s_P(t)]^T \in \Re^P$ distributed on the cortical surface can be related by

$$\mathbf{m}(t) = \mathbf{L}\mathbf{s}(t) + \mathbf{n}(t), \tag{2}$$

where $m_c(t)$ is the temporal waveform measured by the cth MEG sensor at time t, $c = 1, 2, \ldots, C$, $\mathbf{L} = [\mathbf{l}_{\theta_1}\ \mathbf{l}_{\theta_2}\ \ldots\ \mathbf{l}_{\theta_P}] \in \Re^{C\times P}$ is the lead field matrix composed of P lead field vectors, $\mathbf{l}_{\theta_P}$, $p = 1, 2, \ldots, P$, each associated with dipole parameters $\boldsymbol{\theta}_p$, $s_p(t)$ is the amplitude of the pth dipole, $\mathbf{n}(t) \in \Re^C$ denotes the additive noise at time t and 'T' indicates the transpose of a matrix or a vector.

2.2. Cortical activation topographies of ICs

Equation (2) describes the source model indicating that MEG measurements $\mathbf{m}(t)$ originate from the superposition of P brain source activity $\mathbf{s}(t) = [s_1(t)\ s_2(t)\ \ldots\ s_P(t)]^T \in \Re^P$. From another aspect, the ICA method decomposes the measurements $\mathbf{m}(t)$ into K ICs, $\mathbf{x}(t) = [x_1(t)\ x_2(t)\ \ldots\ x_K(t)]^T \in \Re^K$, $K \leqslant C$, in which every component is temporally independent of the others. The measurements $\mathbf{m}(t)$ are weighted superpositions of K ICs, which can be divided into signal and noise subsets. Without loss of generality, we assume that the signal subset $\mathbf{x}_\mathrm{s}(t) = [x_1(t)\ x_2(t)\ \ldots\ x_Z(t)]^T$ contains the first Z components whereas the noise subset $\mathbf{x}_\mathrm{n}(t) = [x_{Z+1}(t)\ x_{Z+2}(t)\ \ldots\ x_K(t)]^T$ contains the remaining $K - Z$ components. That is,

$$\mathbf{m}(t) = \mathbf{A}\mathbf{x}(t) = \mathbf{A}_\mathbf{s}\mathbf{x}_\mathbf{s}(t) + \mathbf{A}_\mathbf{n}\mathbf{x}_\mathbf{n}(t), \tag{3}$$

where $\mathbf{A} = [\mathbf{a}_1\ \mathbf{a}_2\ \ldots\ \mathbf{a}_K] \in \Re^{C\times K}$ is a mixing matrix and its column vector $\mathbf{a}_k$ represents the scalp topography corresponding to the kth component $x_k(t)$. Each scalp topography $\mathbf{a}_k$ is associated either with signal subset $\mathbf{A}_\mathrm{s} = [\mathbf{a}_1\ \mathbf{a}_2\ \ldots\ \mathbf{a}_Z]$ or noise subset $\mathbf{A}_\mathrm{n} = [\mathbf{a}_{Z+1}\ \mathbf{a}_{Z+2}\ \ldots\ \mathbf{a}_K]$. Let $\mathbf{m}_{s_k}(t) = \mathbf{a}_k x_k(t)$ denote the part of the measurements contributed by the temporal profile $x_k(t)$ and the scalp topography $\mathbf{a}_k$ of the kth IC, $k = 1, 2, \ldots, Z$. Let $\mathbf{m}_\mathrm{n}(t) = \mathbf{A}_\mathrm{n}\mathbf{x}_\mathrm{n}(t) \in \Re^C$ denote the part of the measurements contributed by noise components. Assume that the partial measurements $\mathbf{m}_{s_k}(t)$ originate from the superposition of the source signals $\mathbf{s}_k(t) = [s_{1k}(t)\ s_{2k}(t)\ \ldots\ s_{Pk}(t)]^T \in \Re^P$, which reflect the

temporal activity of the dipole sources distributed on the cortical surface. Equation (3) can then be rewritten as

$$\mathbf{m}(t) = \mathbf{A}_s\mathbf{x}_s(t) + \mathbf{A}_n\mathbf{x}_n(t) = \sum_{k=1}^{Z}\mathbf{m}_{s_k}(t) + \mathbf{m}_n(t) = \sum_{k=1}^{Z}\mathbf{L}\mathbf{s}_k(t) + \mathbf{m}_n(t). \quad (4)$$

Note that the noise term $\mathbf{n}(t)$ is not explicitly modeled in (4) but is implicitly embedded in the measurements $\mathbf{m}_n(t)$ contributed by the noise components $\mathbf{x}_n(t)$ (Tsai *et al* 2006).

Let vector $\mathbf{b}_k = [b_{1k}\ b_{2k}\ \ldots\ b_{Pk}]^T \in \Re^P$ represent the cortical activation topography of the kth signal component, $x_k(t)$, $k = 1, 2, \ldots, Z$. The dipole activity $\mathbf{s}_k(t)$ and the signal component $x_k(t)$ can be related by (Tsai *et al* 2006)

$$\mathbf{s}_k(t) = \mathbf{b}_k x_k(t). \quad (5)$$

By substituting (5) into the forward model, equation (4) becomes

$$\mathbf{m}(t) = \sum_{k=1}^{Z}\mathbf{L}\mathbf{b}_k x_k(t) + \mathbf{m}_n(t) = \mathbf{L}\mathbf{B}\mathbf{x}_s(t) + \mathbf{m}_n(t), \quad (6)$$

where $\mathbf{B} = [\mathbf{b}_1\ \mathbf{b}_2\ \ldots\ \mathbf{b}_Z] \in \Re^{P\times Z}$. According to (4) and (6), the relationship between cortical activation topographic matrix $\mathbf{B}$ and scalp topographic matrix $\mathbf{A}_s$ of signal components $\mathbf{x}_s(t)$ can be expressed as the linear equation

$$\mathbf{A}_s\mathbf{x}_s(t) = \mathbf{L}\mathbf{B}\mathbf{x}_s(t). \quad (7)$$

When the data acquisition period is long enough, we can assume that the set of signals $\mathbf{x}_s(t)$ at every time point span the space of $\Re^Z$. Equation (7) is thus equivalent to

$$\mathbf{A}_s = \mathbf{L}\mathbf{B}, \quad (8)$$

or

$$\mathbf{a}_k = \mathbf{L}\mathbf{b}_k, \quad k = 1, 2, \ldots, Z. \quad (9)$$

To obtain a unique and stable solution, the Tikhonov regularization term (Tikhonov and Arsenin 1977) is added to the linear model as in (9) to impose the minimum norm constraint on cortical activation topography $\mathbf{b}_k$. This regularization term can avoid the overfitting problem and provide a solution to the estimation of cortical activation topography $\mathbf{b}_k$ according to the design of the Tikhonov matrix $\mathbf{T}$, which is expressed as

$$\hat{\mathbf{b}}_k = \arg\min_{\mathbf{b}_k}\left\{\left\|\mathbf{C}_n^{-1/2}(\mathbf{a}_k - \mathbf{L}\mathbf{b}_k)\right\|^2 + \lambda\left\|\mathbf{T}\mathbf{b}_k\right\|^2\right\}, \quad (10)$$

where $\mathbf{C}_n \in \Re^{C\times C}$ is the noise covariance matrix and λ is a hyperparameter for balancing the different scales between the fitting residual $\left\|\mathbf{C}_n^{-1/2}(\mathbf{a}_k - \mathbf{L}\mathbf{b}_k)\right\|$ and the regularization term $\|\mathbf{T}\mathbf{b}_k\|$. In the present study, we make no prior assumptions in the estimation of cortical activity, and thus the identity matrix, $\mathbf{I}$, is adopted as the Tikhonov matrix (Hämäläinen and Ilmoniemi 1994, Hauk 2004). Finally, the cortical activation topography $\mathbf{b}_k$ can be calculated by

$$\hat{\mathbf{b}}_k = \left(\mathbf{L}^T\mathbf{C}_n^{-1}\mathbf{L} + \lambda\mathbf{I}\right)^{-1}\mathbf{L}^T\mathbf{C}_n^{-1}\mathbf{a}_k. \quad (11)$$

According to the matrix inversion lemma, we can derive another form of the solution:

$$\hat{\mathbf{b}}_k = \mathbf{L}^T(\mathbf{L}\mathbf{L}^T + \lambda\mathbf{C}_n)^{-1}\mathbf{a}_k. \quad (12)$$

Equation (12) is preferable for estimating $\mathbf{b}_k$ because (12) has only one matrix inverse computation and the dimension of $\mathbf{L}\mathbf{L}^T$, $C \times C$, is usually much smaller than that of $\mathbf{L}^T\mathbf{L}$, which is $P \times P$.

In summary, the proposed method is capable of estimating the cortical activation topography $\mathbf{b}_k$ mapped on the cortical surface through the scalp topography $\mathbf{a}_k$ and the lead field matrix $\mathbf{L}$, once the kth IC, $x_k(t)$, is obtained by ICA.

2.3. Selection of functional components

The proposed component selection methods incorporate the information of the cortical activation topographies, $\mathbf{b}_k$, and the temporal profiles of ICs, $x_k(t), k = 1, 2, \ldots, Z$, to determine the functional components, as illustrated in the flow diagram shown in figure 1. For the kth IC, we first calculate the power of its temporal activity, $E\{(b_{pk}x_k(t))^2\}$, at the pth vertex, where $E\{\cdot\}$ denotes the expectation value. Let $\mathbf{u}_k = [u_{1k}\ u_{2k}\ \ldots\ u_{Lk}]^T$ represent the parceled activity of the L automated anatomical labeling (AAL) regions for the kth IC. The AAL regions for each subject can be obtained by spatially transforming the CH2 template to the MR image of the subject using the registration technique proposed by Liu *et al* (2010). This method utilizes brain structure information to calculate the affine transformation and non-rigid deformation between the CH2 template and the MR image of the subject. These two transformations are then applied to transform the locations of AAL regions from the space of the CH2 template to that of the subject image. For the lth element of $\mathbf{u}_k$, u_{lk}, the value is calculated as the square root of the mean of the α highest power values among the vertices in the lth AAL region. For each AAL region, if α is larger than the number of vertices in that region, then α is adjusted to be the total number of vertices in that region. The parceled activity for all components is calculated and grouped as $\mathbf{U} = [\mathbf{u}_1\ \mathbf{u}_2\ \ldots\ \mathbf{u}_Z]$. Note that the corresponding brain atlas of CH2 template is used to parcel the cortical activation topography of each IC. In contrast, the template used in the template-based IC selection methods defines the characteristics of a specific IC category (De Martino *et al* 2007, Lee *et al* 2003, Wessel and Ullsperger 2011).

We propose two methods to select functional components from the signal subset, $\mathbf{x}_s(t) = [x_1(t)\ x_2(t)\ \ldots\ x_Z(t)]^T$, according to their corresponding parceled activity. The aim of the first method, dominant component selection, is to identify regions with a high degree of activity as well as the components that contribute to this activity. As shown in figure 1(a), the component with the maximum parceled activity among the Z components is first identified for each of the L AAL regions. These L AAL regions are then selected one by one in descending order of amplitude of the maximum parceled activity until the cumulative portion of the maximum parceled activity exceeds $\beta\%$. The selected regions are referred to as dominant regions and the components corresponding to the maximum parceled activity in these regions are referred to as dominant components.

In a dominant region, there may be multiple components with a high degree of activity. Important information may

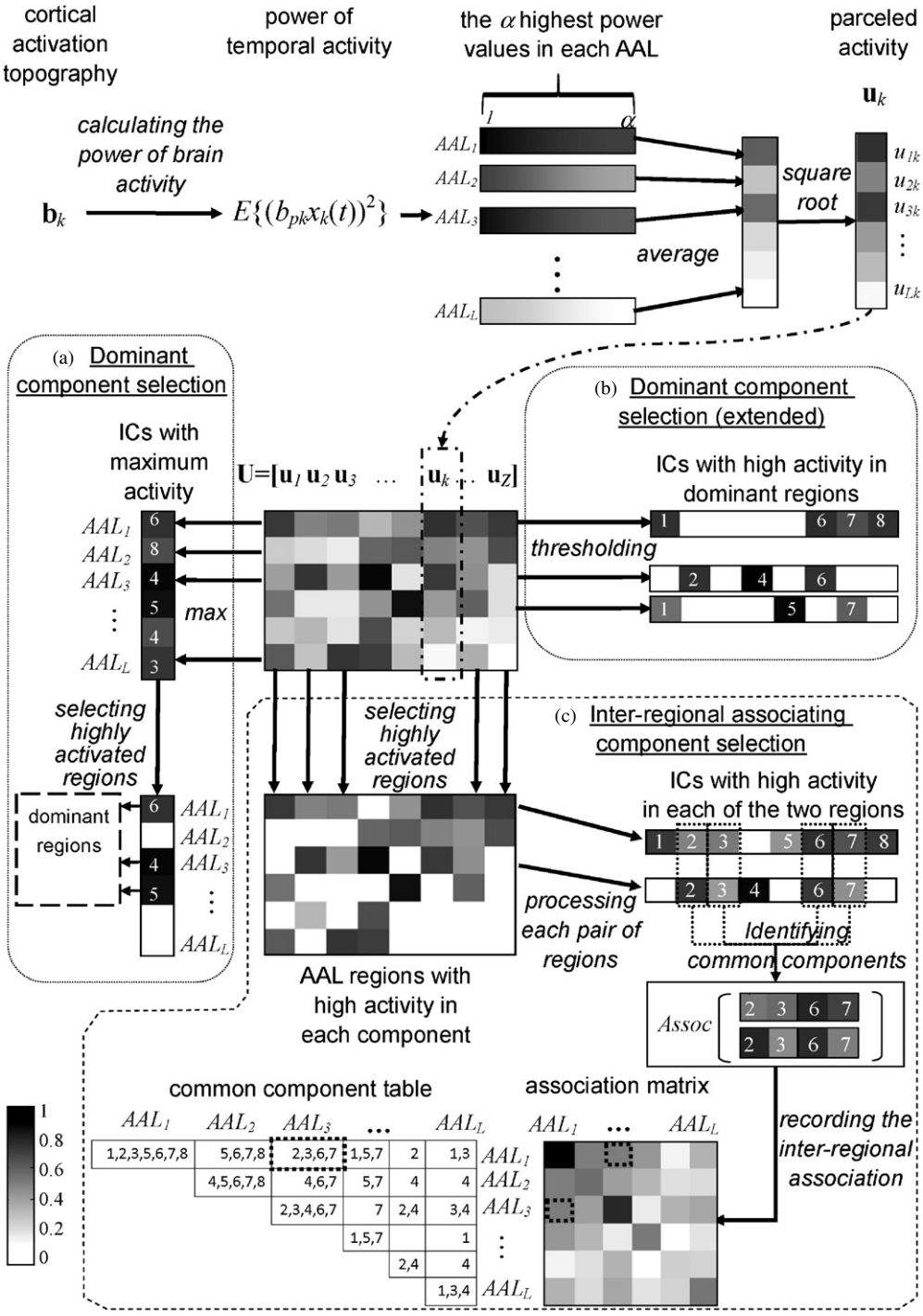

Figure 1. Flow diagram of the proposed component selection methods based on parceled brain activity. For example, the values of L and Z are 6 and 8, respectively, in this diagram. The proposed dominant component selection method is shown in (a) and the selected dominant regions are AAL regions 1, 3 and 4 with dominant components 6, 4 and 5, respectively. The extension of this method is shown in (b) and the extended dominant components selected for dominant regions 1, 3 and 4 are component sets {1, 6, 7, 8}, {2, 4, 6}, and {1, 5, 7}, respectively. As shown in (c), a set of inter-regional associating components {2, 3, 6, 7} designated in the dashed box are the common components between AAL regions 1 and 3, with a strong association between these two regions.

be lost if we only choose the component with the maximum activity using the above-mentioned dominant component selection method. The remedy is to extend this method by reexamining the Z components with a threshold for each dominant region, as shown in figure 1(b). In this extension, components with a relatively high degree of parceled activity are selected from all of the Z components. For a dominant region, the Z components are selected one by one according to their amplitudes of parceled activity sorted descendingly. The selection process terminates when the cumulative portion of parceled activity of the selected components exceeds a certain value. Finally, each dominant region has a set of extended

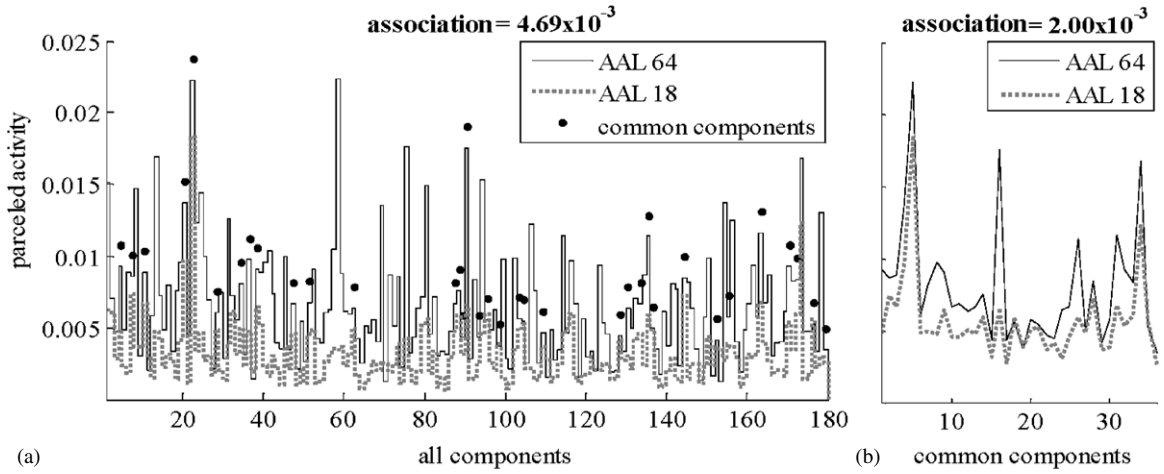

Figure 2. Component spectra of (a) independent components and (b) common components for the right RO (AAL 18) and right SMG (AAL 64). The black dots in (a) indicate the common components of the right RO and right SMG. The association values between the two regions shown at the top of (a) and (b) are calculated as the inner products of their parceled activity in all 179 ICs and the 36 common components, respectively.

dominant components, which contribute to the major portion of brain activity in this region.

The goal of the second component selection method is to select inter-regional associating components, as shown in figure 1(c). Only the pair of regions with a large inter-regional association has associating components, comprising a set of common components for these two regions. For a pair of regions, the common components are the ICs with a high degree of parceled activity in both regions. To select common components, highly activated regions of each IC are first identified according to the parceled activity of each region (regional activity). For each IC, these highly activated regions are selected one by one in descending order of regional activity until the cumulative portion of the regional activity of the selected regions exceeds a given threshold (30% in this study). Then, for each pair of regions, an IC is identified as a common component if its highly activated areas contain both regions. As illustrated in figure 2, the component spectrum of a given region is the amplitude distribution of the parceled activity across components with respect to that region. The association between two brain regions is assessed as the scalar product of their common component spectra, which is a similarity measure of the common components between the two involved brain regions. The association values and common components for all pairs of regions constitute the association matrix and the common component table, respectively. Finally, for a pair of regions with a high degree of association, their common components are regarded as the inter-regional associating components of these two regions.

Note that, for each IC, different brain areas have the same temporal waveform, albeit on different scales. That is, two regions probably connect to each other when both have strong activation in the same IC. Therefore, a large scalar product value of common component spectra can be considered as a high degree of connectivity between two regions because of their similar activation patterns across the components with strong activation.

2.4. Materials

This study recorded MEG signals of a 35-year-old female subject undertaking a gender discrimination experiment. The measurements were acquired using 204-channel gradiometers of a whole-head Neuromag Vectorview system with a sampling rate of 1 kHz. The magnetometers of the Neuromag Vectorview system were not used in our experiments because of their disadvantages of wide field spread (Hyvärinen *et al* 2010) and high sensitivity to noise. The T1-weighted MR images of this subject were acquired on a 1.5 tesla GE MR scanner (3D-FSPGR pulse sequence, TE = 1.828 ms, TR = 8.54 ms, flip angle = 15°, matrix size = $256 \times 256 \times 124$, voxel size = $1.02 \times 1.02 \times 1.50$ mm^3). The cortical surface comprising approximately one hundred thousand vertices was reconstructed from the MR images by FreeSurfer (Dale *et al* 1999).

2.4.1. Simulated measurements. Five sets of simulated 204-channel MEG data were generated using a forward model built for the above-mentioned Vectorview MEG system. In simulations 1, 2a, 2b, and 2c, each dataset had its own configuration containing two dipoles with known parameters. In the configuration of simulation 1, two distant dipoles with parameters $\boldsymbol{\theta}_1 = \{\mathbf{r}_1, \mathbf{q}_1\}$ and $\boldsymbol{\theta}_2 = \{\mathbf{r}_2, \mathbf{q}_2\}$ were placed at $\mathbf{r}_1$ and $\mathbf{r}_2$ and associated with surface-constrained orientations $\mathbf{q}_1$ and $\mathbf{q}_2$, respectively, as shown in the top left of figure 3. In contrast, in the configuration of simulations 2a, 2b and 2c, two close dipoles with parameters $\boldsymbol{\theta}_3 = \{\mathbf{r}_3, \mathbf{q}_3\}$ and $\boldsymbol{\theta}_4 = \{\mathbf{r}_4, \mathbf{q}_4\}$ were deployed at $\mathbf{r}_3$ and $\mathbf{r}_4$ and associated with surface-constrained orientations $\mathbf{q}_3$ and $\mathbf{q}_4$, respectively, as shown in the top right of figure 3. In the configuration of simulation 3, there were five dipoles with parameters $\boldsymbol{\theta}_1$, $\boldsymbol{\theta}_2$, $\boldsymbol{\theta}_3$, $\boldsymbol{\theta}_4$ and $\boldsymbol{\theta}_5 = \{\mathbf{r}_5, \mathbf{q}_5\}$. In simulations 1, 2a, 2b and 2c, the two temporal profiles, waveforms 1 and 2 shown at the top of figure 3, were designed as the source activity whereas waveforms 3, 4, 5 and 6 shown in figure 4(a) were designed as the source activity in simulation 3. Each temporal waveform

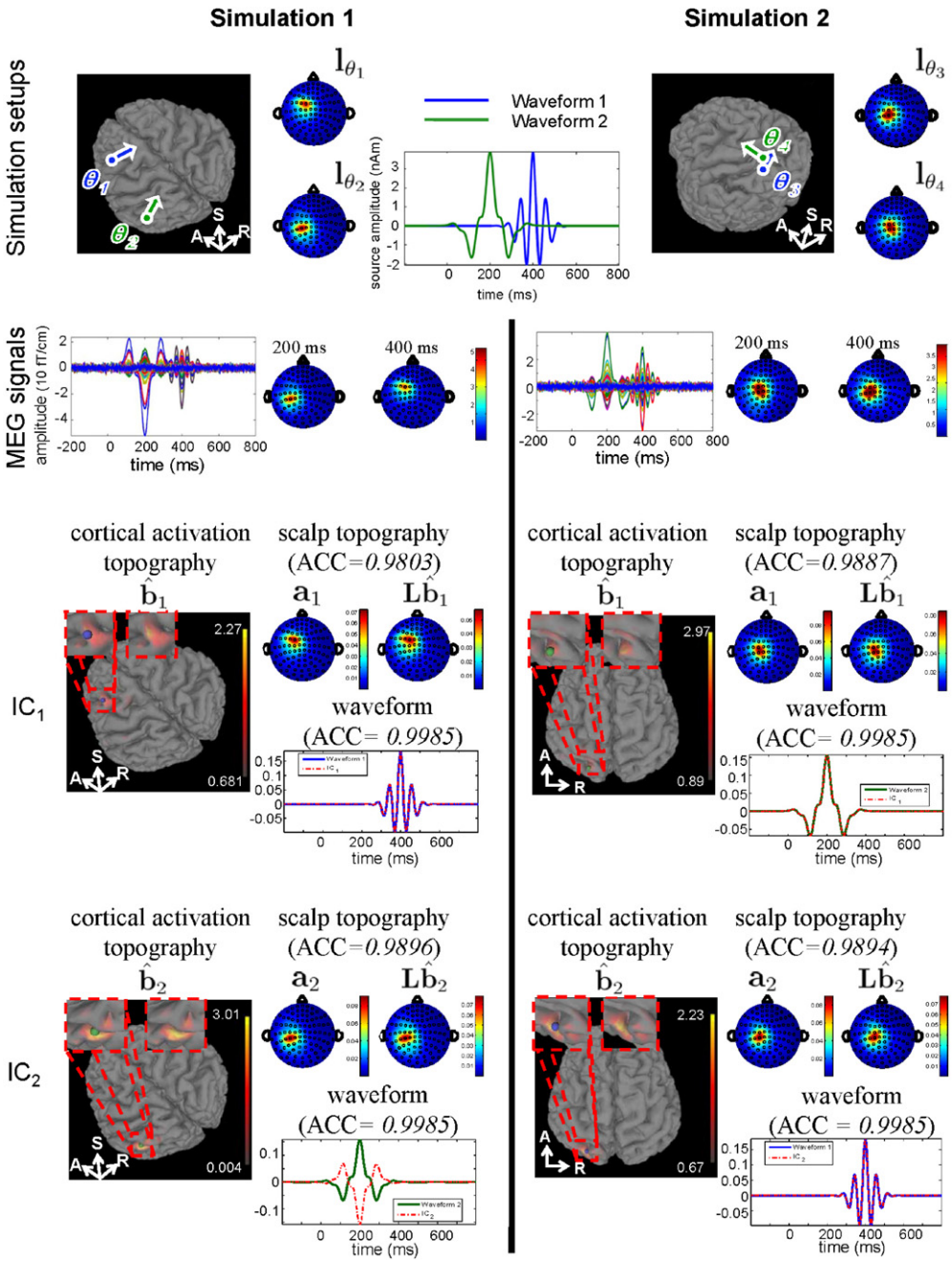

Figure 3. Setups and results of simulations 1 and 2a. Two dipoles for generating MEG data in simulations 1 and 2a are shown top left and top right, respectively. Parameters of these four dipoles are denoted by $\boldsymbol{\theta}_1$, $\boldsymbol{\theta}_2$, $\boldsymbol{\theta}_3$ and $\boldsymbol{\theta}_4$ and their corresponding lead field vectors are denoted by $\mathbf{l}_{\theta_1}$, $\mathbf{l}_{\theta_2}$, $\mathbf{l}_{\theta_3}$ and $\mathbf{l}_{\theta_4}$, respectively. The top middle illustrates two given temporal waveforms, in which waveform 1 is associated with dipoles $\boldsymbol{\theta}_1$ and $\boldsymbol{\theta}_3$ whereas waveform 2 is associated with dipoles $\boldsymbol{\theta}_2$ and $\boldsymbol{\theta}_4$. The second row shows the averaged MEG measurements and the corresponding scalp topographies at 200 ms and 400 ms for the two simulations. The bottom shows temporal waveforms and scalp topographies of the two ICs decomposed from each simulation dataset as well as their corresponding cortical activation topographies. The ACC between the scalp topography of the kth IC, $\mathbf{a}_k$, and the scalp projection of the estimated cortical activation topography, $\mathbf{L}\hat{\mathbf{b}}_k$, is shown in the bracket as well as the ACC between the temporal waveform of IC and its corresponding source activity.

consisted of one or two amplitude-modulated cosine waves formulated as

$$\omega_\rho(t) = a\cos(2\pi f(t-p))G(t;p,\sigma) + n_s(t;\sigma_n), \qquad (13)$$

where the parameter set $\rho = \{a, f, p, \sigma, \sigma_n\}$ contained the amplitude a (nAm), the frequency f (Hz), and the peak time p (ms). The amplitude modulation function $G(t;p,\sigma) = \exp(-(t-p)^2/2\sigma^2)$ was a Gaussian function with standard deviation σ (ms). The interference $n_s(t;\sigma_n)$ added to the cosine wave was the random signal with standard deviation σ_n (nAm). Waveforms 1 and 2 were both ensembles of two amplitude-modulated cosine waves with parameter sets $\{\{3, 17, 400, 50, 0\}, \{0.9, 5, 400, 50, 0\}\}$ and $\{\{3, 5, 200, 70, 0\}, \{0.9, 17, 200, 70, 0\}\}$, respectively, as shown in the top center of figure 3. Waveforms 3, 4 and 6 were all ensembles of two amplitude-modulated cosine waves with parameter sets

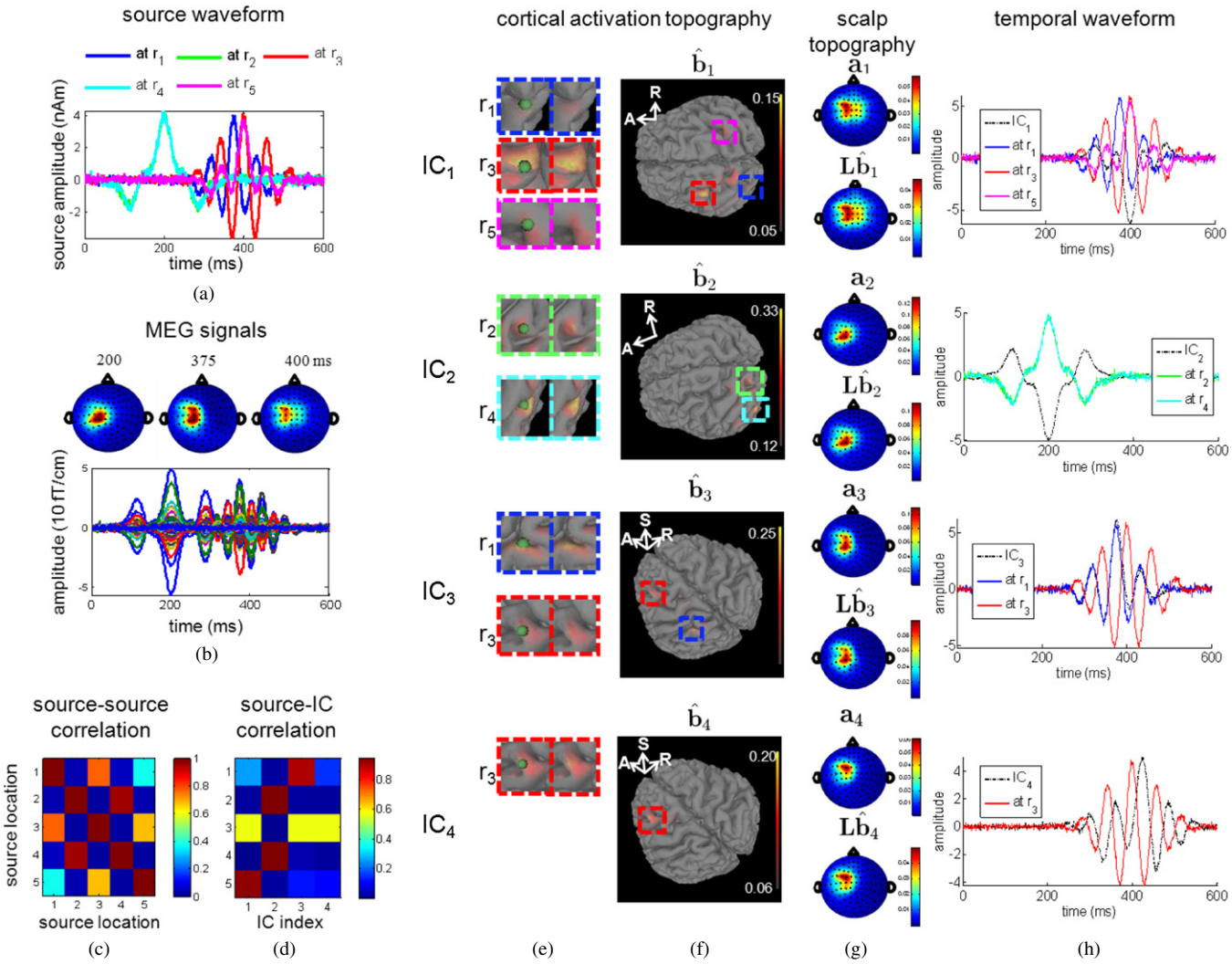

Figure 4. Configuration and results of simulation 3. The waveforms placed at the five locations $\mathbf{r}_1$, $\mathbf{r}_2$, $\mathbf{r}_3$, $\mathbf{r}_4$ and $\mathbf{r}_5$ are shown in (a) and their ACCs are shown in (c). The generated measurements and the corresponding scalp topographies at 200, 375 and 400 ms are shown in (b). The correlation matrix in (d) illustrates the ACCs between the waveforms placed at the five locations and the four ICs decomposed from the simulation dataset. In (e)–(h), each row displays (f) the cortical activation topography, (g) the scalp topographies, and (h) the temporal waveforms for each of the four ICs. The enlarged cortical activation topographies are shown in (e). The green nodes within the dashed boxes colored blue, light green, red, cyan and purple indicate the ground truth dipole locations $\mathbf{r}_1$, $\mathbf{r}_2$, $\mathbf{r}_3$, $\mathbf{r}_4$ and $\mathbf{r}_5$, respectively. Note that the waveforms of the dipoles located at $\mathbf{r}_2$ (light green) and $\mathbf{r}_4$ (cyan) almost overlap each other because they consist of the same amplitude-modulated cosine waves and different realizations of the same random noise process.

{{3, 17, 375, 50, 0.1}, {0.9, 5, 375, 50, 0.1}}, {{0.9, 17, 200, 70, 0.1}, {3, 5, 200, 70, 0.1}} and {{1.8, 17, 400, 50, 0.1}, {1.8, 5, 400, 50, 0.1}}, respectively. Waveform 5 was an amplitude-modulated cosine wave with the parameter set {4, 17, 400, 60, 0.1}, as shown in figure 4(a). For the six source waveforms, 1–6, their associated dipole parameters in each simulation study are listed in table 1. The correlations between the waveforms used in simulation 3 are illustrated in figure 4(c).

To simulate the background activity of the brain, 3000 additional dipoles were randomly deployed within a sphere with a radius of 7 cm centered in the middle of the brain. In simulations 1, 2a and 3, the amplitude of each random dipole was drawn from a normal distribution with zero mean and standard deviation of 0.1 nAm. In simulations 2b and 2c, the data were designed to have a higher level of background noise than in simulation 2a. Each added random dipole had its amplitude drawn from a normal distribution with zero mean and standard deviation of 1 (simulation 2b) or 10 nAm (simulation 2c). To simulate sensor noise, random signals drawn from a normal distribution with zero mean and standard deviation of 10 fT cm^{-1} were added to each channel of MEG signals in simulation 3. Table 1 lists the maximum and mean of the channel-wise signal-to-noise ratio (SNR) for each dipole source of the five sets of simulation data. The spherical model was adopted as the head model in the calculation of the gain matrix. Ten concatenated trials, each with 1000 ms 204-channel data, were generated in this study. In each simulation study, we first performed FastICA (Hyvärinen and Oja 2000) to attenuate interference in the simulated MEG data by removing noise components and then mixing the remaining components. Next, the de-noised measurements were again decomposed

Table 1. Channel-wise SNR (unit: dB) and localization error (LE) for each dipole source in the simulation studies. When a dipole source is correlated with multiple components, its LEs are calculated for each of the estimated cortical activation topographies of the correlated ICs.

Simulation	Std of random dipole (nAm)	Waveform	Dipole parameter	Max SNR (dB)	Mean SNR (dB)	LE (mm)
1	0.1	1	$\boldsymbol{\theta}_1$	17.9	−0.2	0
		2	$\boldsymbol{\theta}_2$	18.7	−0.5	0
2a	0.1	1	$\boldsymbol{\theta}_3$	15.1	−0.7	0
		2	$\boldsymbol{\theta}_4$	18.3	1.5	0
2b	1	1	$\boldsymbol{\theta}_3$	−4.9	−20.7	0
		2	$\boldsymbol{\theta}_4$	−1.7	−18.5	0
2c	10	1	$\boldsymbol{\theta}_3$	−24.9	−40.7	0
		2	$\boldsymbol{\theta}_4$	−21.7	−38.5	0
3	0.1	3	$\boldsymbol{\theta}_1$	11.3	−2.5	0, 0
		4	$\boldsymbol{\theta}_2$	11.5	−1.5	0
		5	$\boldsymbol{\theta}_3$	15.2	0.2	0, 0, 0
		4	$\boldsymbol{\theta}_4$	11.6	−3.5	1.4
		6	$\boldsymbol{\theta}_5$	8.2	−5.4	0.8

into ICs using FastICA. The proposed method was then performed to estimate the cortical activation topographies of these newly obtained ICs.

2.4.2. Gender discrimination experiment. The MEG data were acquired from a gender discrimination study (Lee *et al* 2010). The subject was presented grayscale photographs of faces showing an angry expression. A total of 72 images were displayed in a pseudorandom order. To avoid explicit recognition or categorization of emotional expressions, the subject was asked to lift her right or left index finger after recognizing the presented face image as female or male, respectively. Each trial comprised a 1500 ms exposure to the image of a face, a 700 ms fixation (a cross), and a 1200 ms response cue (a question mark).

In this study, we applied the proposed methods to analyze the dataset acquired in the gender discrimination experiment. This dataset comprised 60 trials without eye movement, each with 500 ms measurements starting from the onset of the display of angry face images. The dataset was first decomposed using FastICA. To attenuate interference in the MEG recordings, components with severely low or high kurtosis values were marked as outlier components and removed (Barbati *et al* 2004). Following the removal of outlier components, the remaining components were remixed as noise-reduced measurements by multiplying their associated columns in the mixing matrix $\mathbf{A}$ and their associated temporal waveforms in $\mathbf{x}(t)$. The remixed signals were then decomposed again using FastICA. For all of the resulting 179 ICs, the proposed method was performed to calculate their cortical activation topographies. For each of the 179 components, we computed the parceled activity, with the parameter α set to be 200, in the AAL regions of the cerebrum, AAL 1, AAL 2, . . . , AAL 90.

3. Results

3.1. Simulation studies

In simulations 1, 2a, 2b and 2c, the de-noised measurements were decomposed into two ICs: IC_1 and IC_2. The bottom of figure 3 illustrates the temporal waveforms and scalp topographies of the ICs as well as the corresponding cortical activation topographies in simulations 1 and 2a. To evaluate the goodness of data fit in our simulation results, the scalp topography of the kth IC, $\mathbf{a}_k$, was compared with the scalp projection $\hat{\mathbf{a}}_k = \mathbf{L}\hat{\mathbf{b}}_k$ of the corresponding cortical activation topography $\hat{\mathbf{b}}_k$, $k = 1$ and 2, using the absolute correlation coefficient (ACC), $\text{ACC} = |\mathbf{a}_k^T \hat{\mathbf{a}}_k|/(\|\mathbf{a}_k\| \cdot \|\hat{\mathbf{a}}_k\|)$. In these two studies, $\mathbf{a}_k$ and $\hat{\mathbf{a}}_k$, $k = 1$ and 2, had the maximum activations located at the same channel and their ACCs were all higher than 0.98, indicating that the estimated cortical activation topographies had scalp projections highly similar to the scalp topographies of the associated ICs.

To evaluate the accuracy of the proposed method for estimating cortical activation topography, we calculated the localization error (LE) for each dipole location, as shown in table 1. The value of LE is calculated as the squared Euclidean distance $\|\mathbf{r}_i - \hat{\mathbf{r}}_i\|^2$ between the peak position $\hat{\mathbf{r}}_i$ on the estimated cortical activation topography and the ground truth position $\mathbf{r}_i$, $i = 1, \ldots, 4$. Note that the positions $\hat{\mathbf{r}}_i$ and $\mathbf{r}_i$ were both located on vertices of the cortical surface. In simulation 1, the temporal profile of IC_1 was highly correlated with waveform 1 (ACC = 0.9985), denoting that IC_1 was associated with the dipole source at $\mathbf{r}_1$, as indicated by the blue node in the left panel of figure 3. For IC_1, the peak position $\hat{\mathbf{r}}_1$ coincided with its ground truth position $\mathbf{r}_1$ and thus its LE was zero. In addition, IC_2 had a temporal profile highly correlated with waveform 2 (ACC = 0.9985) and thus it was associated with the dipole source at $\mathbf{r}_2$, which is indicated by the green node. The LE of the estimated cortical activation topography for IC_2 was also zero. For IC_1 in simulation 2a, the peak position $\hat{\mathbf{r}}_4$ coincided with its ground truth position $\mathbf{r}_4$, which is indicated by the green node in the right panel of figure 3. The estimated cortical activation topography of IC_2 had its peak located at $\hat{\mathbf{r}}_3$, which coincided with the ground truth position of dipole source at $\mathbf{r}_3$, as indicated by the blue node in the cortical activation topography $\hat{\mathbf{b}}_2$. In simulations 2b and 2c, the LEs of the estimated cortical activation topographies for the two ICs were both zero, as shown in table 1.

In simulation 3, four ICs were decomposed from the simulated dataset contributed by five dipole sources. According to the source–IC correlation matrix shown in figure 4(d), each component had high correlation values with multiple sources, except for IC_4. The waveform of the dipole placed at $\mathbf{r}_1$ was correlated to the temporal waveforms of IC_1 and IC_3 (with correlation values higher than 0.2), whereas the waveform of the dipole placed at $\mathbf{r}_3$ was correlated to the temporal waveforms of IC_1, IC_3, and IC_4 (with correlation values higher than 0.2). For the dipole sources at $\mathbf{r}_1$ and $\mathbf{r}_3$, their LEs were calculated in each of the cortical activation topographies of their correlated ICs. The LEs of the five sources in simulation 3 are listed in table 1. Figure 4(f) displays the estimated cortical activation topographies of the four ICs.

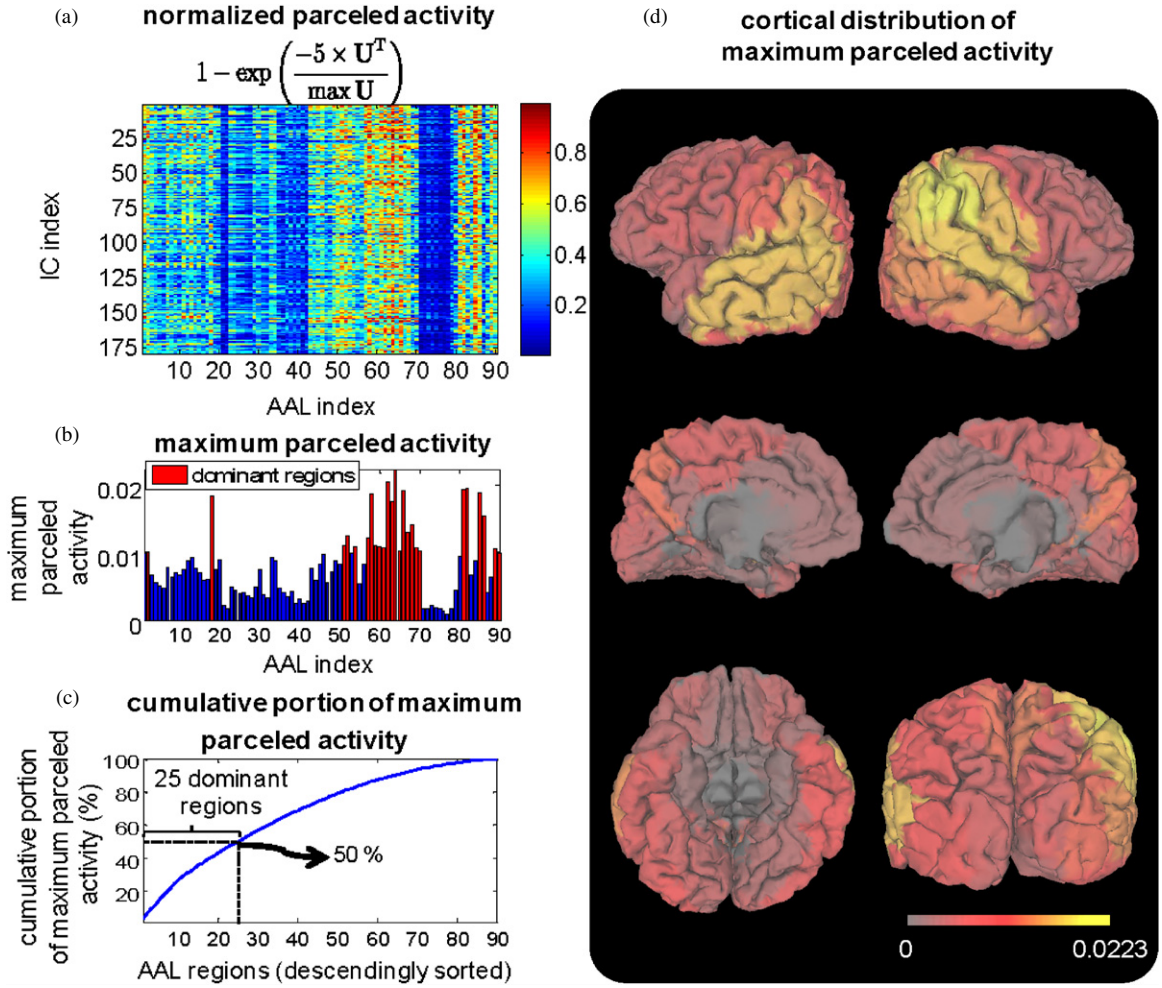

Figure 5. Parceled activity and the determination of dominant regions in the gender discrimination study. The parceled activity of the 179 ICs decomposed from the gender discrimination data is illustrated in (a). The maximum parceled activity of regions is illustrated as the bar chart in (b) and the corresponding cortical activation topographies are shown in (d). The activity is sorted in descending order and the cumulative portion of maximum activity is shown in (c). Red bars in (b) indicate the selected dominant regions containing 50% cumulative portion of the maximum parceled activity.

In figure 4(e), the blue, light green, red, cyan and purple dashed boxes display the enlarged cortical activation topographies with the green nodes indicating the ground truth positions $\mathbf{r}_1$, $\mathbf{r}_2$, $\mathbf{r}_3$, $\mathbf{r}_4$ and $\mathbf{r}_5$, respectively. In this study, the ACC values of $\mathbf{a}_k$ and $\hat{\mathbf{a}}_k$, $k = 1, 2, 3$ and 4, were all higher than 0.98.

3.2. Gender discrimination study

3.2.1. Selected dominant components. Among the parceled activity of the 179 components (figure 5(a)), the amplitude of maximum parceled activity for each AAL region was first identified, as illustrated by a bar chart (figure 5(b)) and cortical distribution (figure 5(d)). We then accumulated the amplitude of maximum parceled activity, which was sorted beforehand in descending order, as shown in figure 5(c). When the cumulative portion of activity reached 50%, 25 regions were included and specified as dominant regions, as indicated by the red bars shown in figure 5(b) and listed in table 2. Most of the dominant regions were in the superolateral parietal, superolateral temporal and occipital regions. The component associated with the maximum parceled activity in a dominant region was identified as the dominant component. The dominant components selected from the 179 ICs are listed in the rightmost column of table 2. Because several dominant regions could be associated with the same components, there were only nine different dominant components in this case.

Figure 6(a) illustrates the temporal waveforms $x_k(t)$ and scalp topographies $\mathbf{a}_k$ of the nine selected dominant components, $k = 1, 2, 8, 22, 24, 26, 58, 150$ and 173. IC_1 with peak latencies at 78, 140 and 285 ms was associated with seven dominant regions, including the bilateral precuneus, superior parietal areas and paracentral lobules, as well as the right precentral area (table 2). Apart from IC_1, each of the other eight dominant components was associated with dominant regions located on the unilateral hemisphere. Left middle occipital gyrus (MOG) was associated with IC_{150} with peak latencies at 87, 130 and 203 ms, whereas right MOG was associated with IC_{173} with peak latencies at 100, 210 and 273 ms. The identified peaks of temporal activity in the left MOG occurred earlier than those in the right MOG. The dominant regions in the temporal lobe of the left hemisphere were associated with IC_2 (superior)

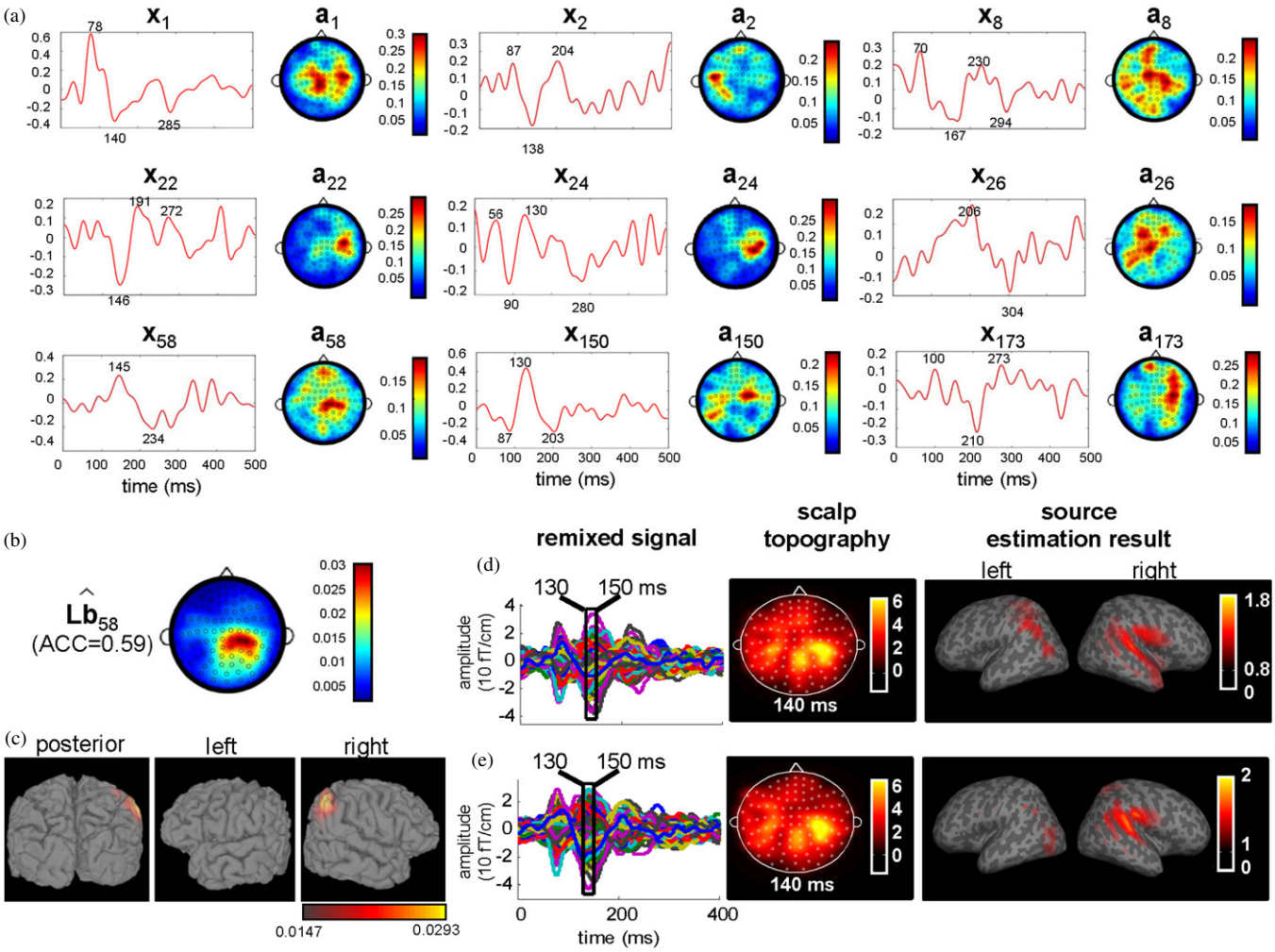

Figure 6. Results of the dominant component selection and the extended dominant component selection method in the gender discrimination study. The temporal waveforms labeled with peak latencies and scalp topographies of dominant components are shown in (a). For IC_{58}, its estimated cortical activation topography and the corresponding scalp projection are illustrated in (c) and (b), respectively. The ACC between the scalp topography $\mathbf{a}_{58}$ and the scalp projection of the estimated cortical activation topography $\mathbf{L}\hat{\mathbf{b}}_{58}$ is shown in parenthesis. For (d) the right SMG and (e) the right IPL, the remixed signals of their extended dominant components are shown on the left. The scalp topographies at peak latency are shown in the middle and their corresponding source distributions estimated by the MCB method are shown on the right.

and IC_8 (middle/inferior), whereas those of the right hemisphere were associated with IC_{22} (superior/inferior) and IC_{24} (middle). The estimated cortical activation topography and the scalp projection of IC_{58} are shown in figures 6(c) and (b), respectively. The ACC value between the scalp projection and the associated scalp topography of IC_{58} was 0.59. The ACC values for the nine dominant components in this study ranged from 0.49 to 0.72.

To reveal the neural network relevant to the selected dominant regions, we applied the extended dominant component selection method to incorporate the components that have a high degree of activity at the given region. There were 67 and 63 dominant components selected for the right supramarginal gyrus (right SMG, AAL 64) and right inferior parietal lobule (right IPL, AAL 62), respectively, in which the cumulative portion of activity reached 60%. Figures 6(d) and (e) depict the signals remixed from the dominant components of the right SMG and IPL, respectively. These two figures also show the scalp topographies at peak latency of 140 ms as well as the source distributions estimated by the MCB method with the time window centered on the peak latency. Each of the two estimated source distributions is overlaid on the inflated cortical surface (Fischl *et al* 1999). The results of MCB are shown as F-statistic maps, which depict the significance levels of brain activity. As illustrated by the F-statistic map in figure 6(d), the neural network associated with the right SMG consists of the SMG, superior temporal gyrus (STG), and Rolandic operculum (RO) in the right hemisphere as well as the left MOG. The F-statistic map in figure 6(e) displays the neural network associated with the right IPL, including the SMG, STG, RO and superior temporal pole in the right hemisphere, as well as the MOG and IPL in the left hemisphere.

3.2.2. Selected inter-regional associating components. In the analysis of inter-regional associating component selection, we found large numbers of common components in the parietal and temporal lobes, particularly when the left MTG, right

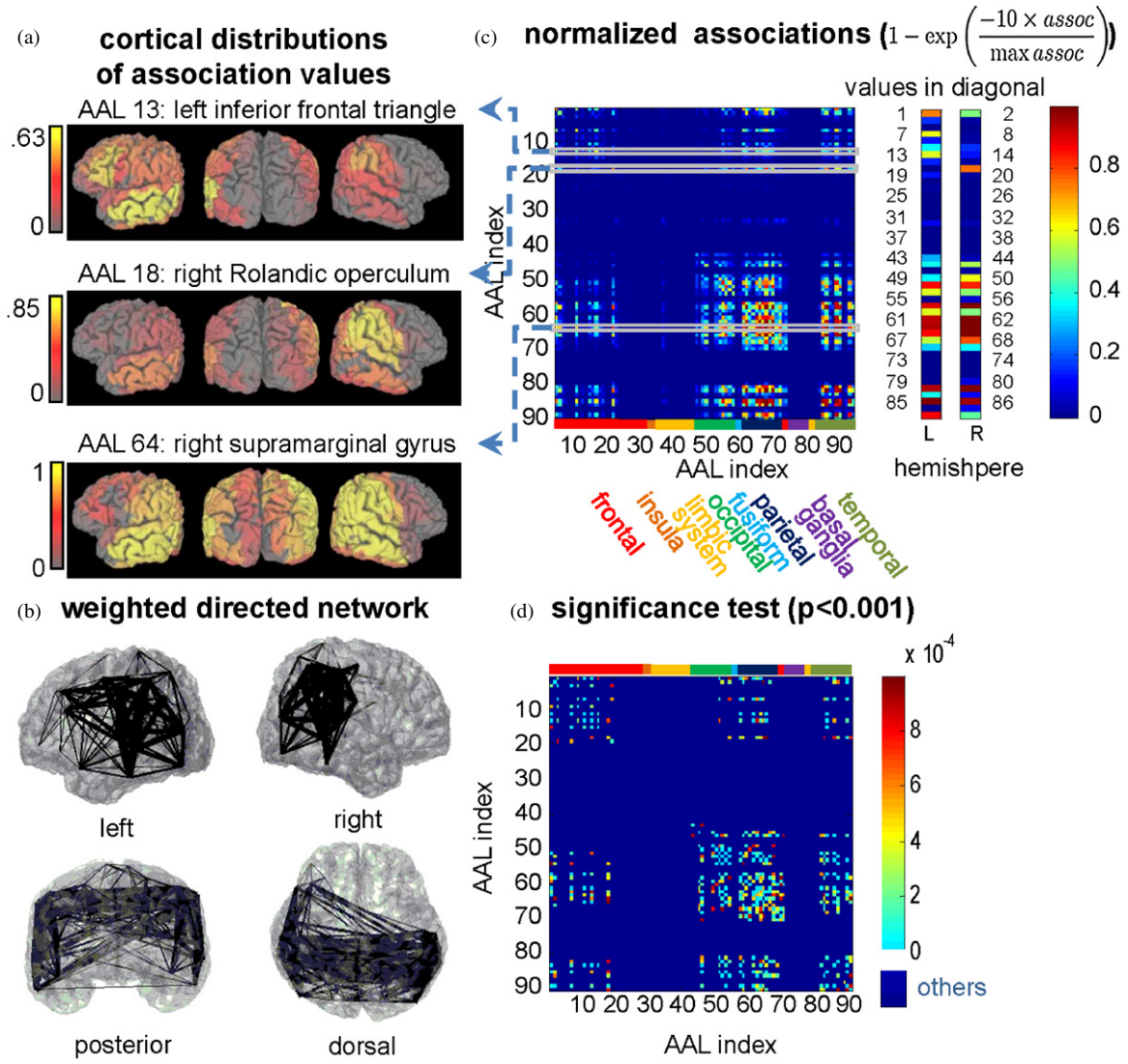

Figure 7. The inter-regional association values and their significance test results in the gender discrimination study. The normalized inter-regional associations calculated from the common components of all regional pairs are shown in (c). Panel (a) displays three cortical distributions of the association values when the left inferior frontal triangle, right RO and right SMG were used as the reference regions. The p-values of these inter-regional association values are shown in (d), where regional pairs surviving $p < 0.001$ are displayed. The functional brain network estimated according to the normalized inter-regional association matrix and their significance level is shown in (b). Two regions are linked when their inter-regional association value is significant ($p < 0.001$). The width of each link represents the strength of association.

SMG, or right angular gyrus (AG) was involved. These three regions had the maximum diagonal values (139, 136 and 110) in the common component matrix, meaning that there were many components with primary activity in these areas. Therefore, most of the ICs extracted from the gender discrimination data were highly activated on the left MTG, right SMG, or right anterior AG.

Figure 2(a) illustrates the parceled activity of right RO (AAL 18) and right SMG (AAL 64) where their common components are indicated with black dots over the top of their corresponding activity. The component spectra of the two regions describe the variations in regional activity across all ICs. Figure 2(b) illustrates the common component spectra for right RO and right SMG. Although only 36 ICs (one-fifth of the total) were selected as the common components, their association value (2.00×10^{-3}) was nearly half of that computed from the total 179 ICs (4.69×10^{-3}).

Figure 7(c) illustrates the inter-regional associations of the common components for all pairs of regions. In general, the inter-regional association value is proportional to the number of common components because the scalar product is used as the similarity measure. In addition, the association value in the diagonal of the association matrix generally represents the power of the activity in a region. The results demonstrate that the activity in the frontal lobe was lateralized to the left hemisphere whereas that in the parietal and temporal lobes was bilaterally distributed. Moreover, high associations were found between the superolateral parietal, superolateral temporal and occipital lobes. These regions with high associations were also found as the dominant regions listed in table 2.

Table 2. Dominant regions together with the corresponding dominant ICs decomposed from the gender discrimination data.

	Dominant AAL region			Normalized maximum	
Rank	Index	Label	Side	activity (%)	Dominant component
1	64	Supramarginal	R	3.13	IC_{58}
2	62	Inferior parietal	R	2.87	IC_{58}
3	82	Superior temporal	R	2.73	IC_{22}
4	81	Superior temporal	L	2.71	IC_{2}
5	66	Angular	R	2.68	IC_{58}
6	85	Middle temporal	L	2.64	IC_{8}
7	58	Postcentral	R	2.61	IC_{22}
8	18	Rolandic operculum	R	2.57	IC_{22}
9	63	Supramarginal	L	2.45	IC_{2}
10	86	Middle temporal	R	2.16	IC_{24}
11	68	Precuneus	R	1.99	IC_{1}
12	67	Precuneus	L	1.83	IC_{1}
13	52	Middle occipital	R	1.75	IC_{173}
14	57	Postcentral	L	1.71	IC_{2}
15	51	Middle occipital	L	1.55	IC_{150}
16	59	Superior parietal	L	1.53	IC_{1}
17	54	Inferior occipital	R	1.53	IC_{173}
18	60	Superior parietal	R	1.51	IC_{1}
19	69	Paracentral lobule	L	1.50	IC_{1}
20	61	Inferior parietal	L	1.50	IC_{26}
21	89	Inferior temporal	L	1.48	IC_{8}
22	65	Angular	L	1.42	IC_{26}
23	70	Paracentral lobule	R	1.41	IC_{1}
24	2	Precentral	R	1.40	IC_{1}
25	90	Inferior temporal	R	1.39	IC_{22}

To evaluate the significance of the inter-regional association value for each regional pair, the p-value was calculated under a permutation distribution. The distribution was built from 1000 000 association values which were calculated from randomly selected components. The percentages of regional pairs having inter-regional association values surviving $p < 0.05$, $p < 0.01$ and $p < 0.001$ were 68.4%, 44.0% and 26.4%, respectively. Figure 7(b) illustrates the weighted undirected network, which was estimated according to the inter-regional association matrix shown in figure 7(c). In this graph, each node represents an AAL region and the link width represents the strength of association. The network only illustrates significant connections whose p-values are smaller than 0.001, as shown in figure 7(d).

We overlaid the cortical surface with the association values when the left inferior frontal triangle, right RO and right SMG were specified as reference regions, as shown in figure 7(a). As can be seen, the left inferior frontal triangle was strongly associated with the left superolateral temporal, superolateral parietal, middle frontal and inferior frontal areas, as well as with the right superolateral parietal and superior temporal areas. The right RO was strongly associated with the regions in the bilateral parietal and temporal lobes. When the left inferior frontal triangle and the right RO were specified as reference regions, most of the regions with the strongest associations were laterally located in the left hemisphere and right hemisphere, respectively.

The left MTG, as shown in figure 8(b), was the region having the highest associations with the left inferior frontal triangle. The remixed signals of their inter-regional associating components, the corresponding scalp topography at peak latency, source distribution at peak latency estimated by MCB, are shown in the three columns from left to right. The F-statistic map in figure 8(b) indicates that the estimated source activity of the remixed signals was left-lateralized on the STG, MTG, MOG, SMG, RO, inferior frontal operculum, inferior frontal triangle, paracentral lobe, cuneus and fusiform gyrus.

4. Discussion

This work proposes a novel technique to facilitate IC selection by estimating the associated cortical activation topography for each IC, which provides spatial information concerning neural activity, together with its temporal profile and scalp topography. Moreover, this technique can further ease IC selection by revealing the dominant components corresponding to dominant regions, which contain major brain activity. By specifying a reference region according to the task of the experiment, this technique can automatically determine the corresponding set of inter-regional associating components as well as the significance level of the association between the reference region and other regions on the cortical surface. Once the functional components are chosen, they can be remixed to reconstruct the neuromagnetic signals for further analysis without the interference of artifactual components.

In the proposed inter-regional associating component selection method, inter-regional association is the scalar product of the two common component spectra for a pair of regions. The value measures the similarity and strength of the activity across components between two regions. The weighted undirected network reflects a graphical visualization of the inter-regional association matrix and may implicitly represent a functional brain network. Compared to the methods using temporal correlation (Gaetz *et al* 1998, Gevins *et al* 1985), our method focuses on the portion of brain activity that contributes to the functional brain networks. The temporal correlation of overall activity may suffer from interference caused by activity outside the targeted networks. Moreover, the temporal waveform of an IC is not necessarily a narrowband signal. Compared to methods using spectral coherence as the measure of connectivity (Gross *et al* 2001), the connectivity constructed using our method would not be constrained within a restricted frequency range. To sum up, the components for a pair of regions selected using our method demonstrate a strong association of network-related activity between these two regions. The connections of the functional brain network estimated using our method, as shown in figure 7(b), also inherit the above characteristics.

The association between a pair of regions is measured by the scalar product of the common component spectra but not by the correlation coefficient of these spectra. To calculate the correlation coefficient, each common component spectrum needs to be normalized. In this case, a pair of regions with few common components may have a higher correlation coefficient value than a region pair with a large number of common components. However, a larger number of common components in two regions may be an indication that more components could have connections between them, and thus

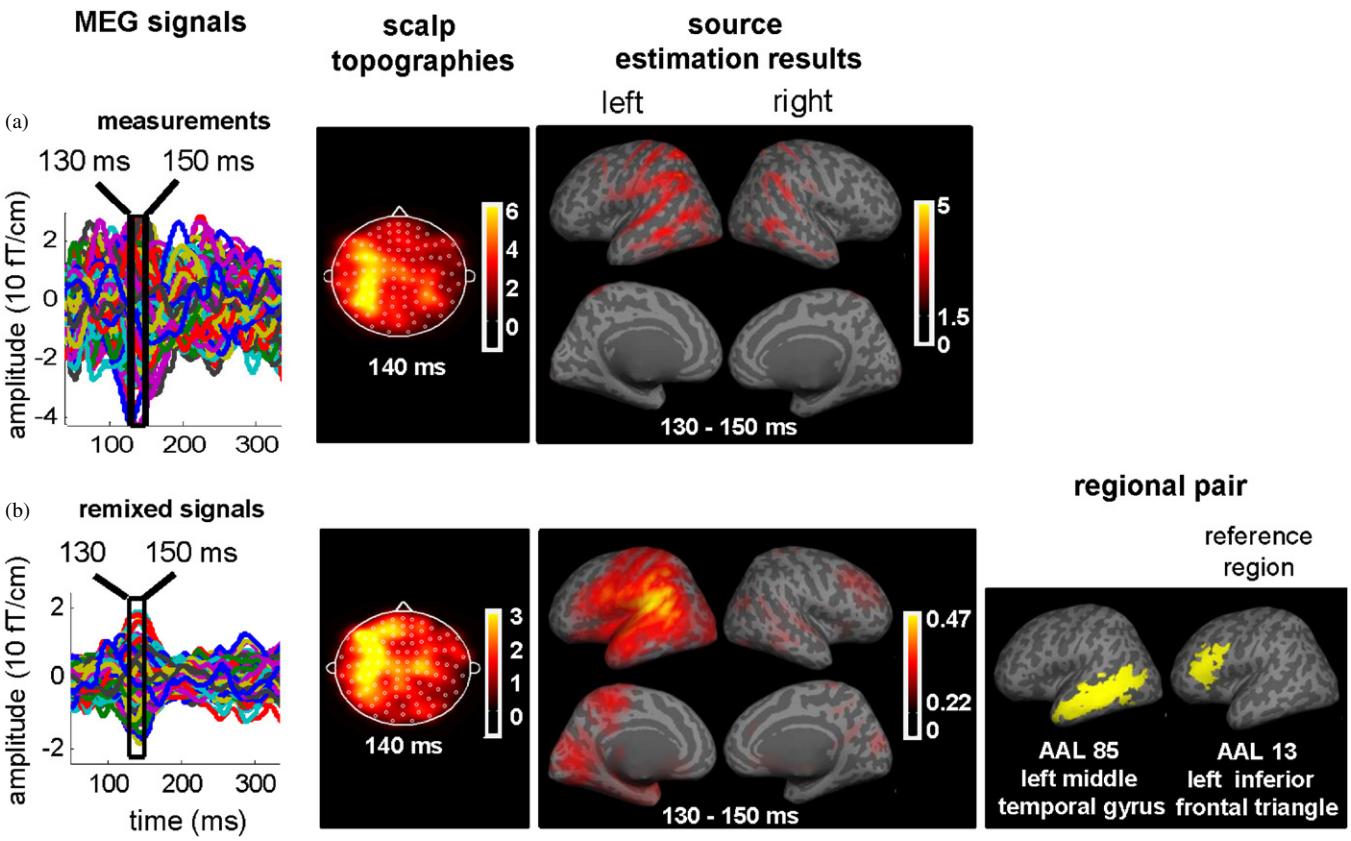

Figure 8. Source estimation results of (a) the MEG data and (b) the signals remixed from the inter-regional associating components of left IFG (triangular part) and left MTG. The four columns from left to right illustrate the MEG signals, scalp topographies at peak latency, source distribution estimated at peak latency, and the pair of regions involved. The black boxes indicate the 20 ms time windows for estimating brain activation sources using the MCB method.

their connectivity may be stronger in the functional brain network. The scalar product of spectra applied to the proposed associating component selection method measures not only the similarity of the spectra but also the cumulative amplitude of the potential connectivity.

In the gender discrimination study, the bilateral superior temporal cortex (STC), bilateral inferior occipital gyrus (IOG), and right MTG were five of the 25 dominant regions selected using the proposed method (table 2). These five dominant regions and the fusiform gyrus (FG) constitute the core system for face perception (Haxby *et al* 2000, 2002). Moreover, the STG, MTG, IOG, together with the frontal operculum and inferior frontal gyrus (IFG), correspond to the perception of facial expressions (Engell and Haxby 2007, Ishai 2008, Said *et al* 2010). The right SMG was also selected as one of the dominant regions. The somatosensory-related cortices comprising the SMG, insula and somatosensory cortex are crucial for recognizing emotions in faces, as reported in various studies on lesions (Adolphs 2002, Adolphs *et al* 1996, 2000). In this study, the proposed selection strategy facilitated the identification of the highly activated regions that can be highly related to visual face perception and early face recognition processes.

The selection of functional components according to the estimated association matrix may be able to facilitate focusing source estimation on brain activity pertaining to specific functions, such as face processing. Fusiform face area plays an essential role in face processing. In the intracranial EEG study (Klopp *et al* 2000), the FG has high coherence with the IFG, MTG, SMG, RO, hippocampus, gyrus rectus, temporal pole, perirhinal cortex and posterior cingulate gyrus in the alpha or gamma band. In the fMRI study (Fairhall and Ishai 2007), the FG had a causal influence on the IFG and amygdala when the visual stimuli contained emotional faces. However, using the source estimation method, such as the MCB method, to analyze the original MEG measurements revealed very weak activity in the FG, as shown by the source distributions in figure 8(a). A probable reason for this is that MEG sensors are less sensitive to activity originating from deep regions than those from superficial regions. FG activity is very likely covered by superimposed superficial brain activity and is thus barely detectable in the original MEG measurements. In our study, the diagonal of the association matrix demonstrated that the left IFG (opercular and triangular parts) had a high degree of activity, as shown in figure 7(c). The IFG plays a crucial role in visual perception with unfamiliar faces, as demonstrated in the intracranial EEG experiment performed by Barbeau *et al* (2008). When the remixed signals of the associating components of the left IFG (triangular part) and left MTG were used for source estimation, the activity of the left FG was revealed, as shown in figure 8(b).

In the extended dominant component selection method, extended dominant components selected for two close regions are generally similar. For example, a total number of 46

dominant components (around 70%) are the same within the total numbers of 68 and 64 extended dominant components of the right SMG and right IPL, respectively. Furthermore, the remixed signals as well as the source estimation results of the extended dominant components in adjacent regions were similar, as shown in figures 6(d) and (e). In addition, the number of common components of adjacent regions is generally large. As a result, between adjacent regions, the inter-regional associations would be generally strong due to the large number of common components. In our study, when the reference region was the right SMG, the regions with the four largest inter-regional associations were the four regions adjoining the right SMG: the right AG, STC, IPL and postcentral gyrus.

In the simulation studies, either with distant or close dipoles, the estimation of cortical activation topography is very accurate in terms of the localization error of peak position. The hyperparameter λ in (12) was set to be small to achieve low fitting residuals, and thus the scalp projections of cortical activation topographies were highly similar to the scalp topographies of the corresponding ICs. Because there was only one dipole source associated with each component, the estimated cortical activation topography of each IC was focally distributed, as illustrated in figure 3. In the gender discrimination study, however, a single component may consist of multiple brain activity sources. We used a larger value for λ in (12) to avoid the problem of over-fitting and thereby smoothing the cortical distribution. Therefore, the scalp projections of the estimated cortical activation topographies may deviate from the scalp topographies of ICs in this case, as shown in figure 6(b).

In the proposed framework, the localization accuracy might be less affected by a high background noise level in MEG/EEG data when the noise is highly independent of source waveforms. At this time, ICA is possible to clearly separate the brain sources from the noise and thus the scalp topography of the IC would have lower interference than the original MEG/EEG measurements. The proposed method inherently stands a good chance of producing a more accurate estimate of cortical activation topography. In the simulation studies, when the standard deviation of the additional random dipole in simulation 2a was enlarged from 0.1 to 1 nAm (simulation 2b) or 10 nAm (simulation 2c), the LEs of the estimated cortical activation topographies corresponding to waveforms 1 and 2 still remained at zero, as shown in table 1.

In this study, the framework of the proposed method for estimating cortical activation topography is based on the l_2-norm with only one constraint, that is, the minimum norm constraint on the cortical activation topography. However, the framework can be extended to a general form based on the l_p-norm. When p is large, the estimated cortical activation topographies tend to be smooth. On the other hand, the l_1-norm is suitable for locating focal sources (Uutela *et al* 1999). When prior information or assumptions about sources (for example, statistical maps estimated from fMRI data) are incorporated, additional anatomical or spatial constraints can be included in this framework to improve estimation accuracy. Moreover, the spatial Laplacian operator can be imposed to obtain smooth cortical activation topographies (Pascualmarqui *et al* 1994). Instead of the identity matrix used in this study, a weighting matrix can be used as the Tikhonov matrix in (10) (Michel *et al* 2004) to attenuate the tendency of estimating superficial sources caused by the minimum norm constraint. For example, one can use a depth-related weighting matrix based on the norms of lead field vectors (Fuchs *et al* 1999). Nevertheless, it should be noted that solving the linear model with multiple constraints or based on l_p-norm with $p \neq 2$ is more difficult than solving the linear model proposed in this study.

The proposed cortical activation topography estimation method can also be used to compute the tomographic activity distribution throughout the entire brain volume, including the subcortical areas. However, the large number of free variables would cause instability in estimation as well as high cost of memory space and computational time. Therefore, this study estimated the cortical activation topography of source distributions only on the cortical surface.

In the proposed component selection method, the parceled activity of each AAL region is the average of a fixed number of the highest power values in that region. Alternatively, the parceled activity can be calculated as the average of a fixed percentage of the highest power values in each region. However, in this way, the parceled activity calculated for a large region tends to be lower than that for a small region when both types of regions have the same number of vertices with high power values.

Instead of the maximum parceled activity, the dominant region can be selected according to the average of parceled activity of all ICs in each region. However, regions with more highly activated components will be more likely to be chosen than regions containing fewer components, even with higher activity. Therefore, the proposed selection method determines the dominant regions based on the ICs with the maximum parceled activity. In this way, the region associated with only a few highly activated components gets a better chance of being considered as a dominant region.

In the proposed inter-regional associating component selection method, the first step is to select highly activated regions for each component so that the cumulative portion of parceled activity for the selected regions reaches 30%. In general, a component with a higher degree of activity (strong component) tends to have more highly activated regions than a component with a lower degree of activity (weak component). If this step is neglected, the strong component will be involved in the inter-regional association calculation for many more pairs of regions. Because the association value is measured by the scalar product of component spectra, the associations will be strongly influenced by the association pattern within strong components and the association pattern occurring within weak components will be covered by the strong components.

Errors in cortical parcellation may result in inaccurate estimation of parceled activity in the proposed component selection method. Parcellation was performed according to the anatomical labels of cortical regions in the MR images of the subject spatially normalized to the template. Therefore, registration error inevitably influences parcellation accuracy, particularly for small regions such as the amygdala.

In addition to FastICA, the proposed methods can also use other kinds of temporal ICA algorithms to decompose electromagnetic recordings, such as COM2 (Comon 1994), ICAR (Albera *et al* 2005), infomax (Bell and Sejnowski 1995, Lee *et al* 1999), JADE (Cardoso and Souloumiac 1993), RobustICA (Zarzoso and Comon 2010), and SOBI (Belouchrani *et al* 1997). In this study, FastICA was used to decompose the measurements because of its high computational efficiency. However, data analysts should choose the appropriate ICA methods according to the characteristics of the datasets (Delorme and Makeig 2004, Kachenoura *et al* 2008, Makeig *et al* 2004) and our method provides this flexibility.

5. Conclusions

This paper presents a framework capable of selecting functional components according to the estimated cortical activation topographies of ICs decomposed by conventional ICA algorithms. Dominant components and inter-regional associating components are selected according to the parcellation of the estimated cortical activation topographies. The associating component selection method provides the inter-regional association and its significance level for each pair of regions by measuring the similarity of their component spectra and strength of their cumulative regional activity. Simulation was used to evaluate the accuracy of the proposed method, whereas the investigation of gender discrimination further demonstrates its effectiveness and practicability. In the analysis of the MEG data acquired during the presentation of angry face image stimuli, our method can provide the functional components and the functional brain network.

Acknowledgments

This work was supported in part by the MOE ATU program, Taiwan National Science Council under grant numbers: NSC-99-2628-E-009-088, NSC-99-2628-E-010-001 and NSC-100-2220-E-009-059, and the UST-UCSD International Center of Excellence in Advanced Bio-engineering sponsored by the Taiwan National Science Council I-RiCE Program under grant number: NSC-99-2911-I-009-101.

References

Adolphs R 2002 Neural systems for recognizing emotion *Curr. Opin. Neurobiol.* **12** 169–77

Adolphs R, Damasio H, Tranel D, Cooper G and Damasio A R 2000 A role for somatosensory cortices in the visual recognition of emotion as revealed by three-dimensional lesion mapping *J. Neurosci.* **20** 2683–90

Adolphs R, Damasio H, Tranel D and Damasio A R 1996 Cortical systems for the recognition of emotion in facial expressions *J. Neurosci.* **16** 7678–87

Albera L, Ferréol A, Chevalier P and Comon P 2005 ICAR: a tool for blind source separation using fourth-order statistics only *IEEE Trans. Signal Process.* **53** 3633–43

Baillet S, Mosher J C and Leahy R M 2001 Electromagnetic brain mapping *IEEE Signal Process. Mag.* **18** 14–30

Barbati G, Porcaro C, Zappasodi F, Rossini P M and Tecchio F 2004 Optimization of an independent component analysis approach for artifact identification and removal in magnetoencephalographic signals *Clin. Neurophysiol.* **115** 1220–32

Barbeau E J, Taylor M J, Regis J, Marquis P, Chauvel P and Liégeois-Chauvel C 2008 Spatio temporal dynamics of face recognition *Cereb. Cortex* **18** 997–1009

Bell A J and Sejnowski T J 1995 An information maximization approach to blind separation and blind deconvolution *Neural Comput.* **7** 1129–59

Belouchrani A, Abed-Meraim K, Cardoso J-F and Moulines E 1997 A blind source separation technique using second-order statistics *IEEE Trans. Signal Process.* **45** 434–44

Cao J T, Murata N, Amari S, Cichocki A and Takeda T 2002 Independent component analysis for unaveraged single-trial MEG data decomposition and single-dipole source localization *Neurocomputing* **49** 255–77

Cao J T, Murata N, Amari S, Cichocki A and Takeda T 2003 A robust approach to independent component analysis of signals with high-level noise measurements *IEEE Trans. Neural Netw.* **14** 631–45

Cardoso J-F and Souloumiac A 1993 Blind beamforming for non-Gaussian signals *IEE Proc. F* **140** 362–70

Chen Y-S, Cheng C-Y, Hsieh J-C and Chen L-F 2006 Maximum contrast beamformer for electromagnetic mapping of brain activity *IEEE Trans. Biomed. Eng.* **53** 1765–74

Comon P 1994 Independent component analysis, a new concept? *Signal Process.* **36** 287–314

Contreras-Vidal J L and Kerick S E 2004 Independent component analysis of dynamic brain responses during visuomotor adaptation *NeuroImage* **21** 936–45

Cuffin B N 1998 EEG dipole source localization *IEEE Eng. Med. Biol. Mag.* **17** 118–22

Dale A M, Fischl B and Sereno M I 1999 Cortical surface-based analysis: I. Segmentation and surface reconstruction *NeuroImage* **9** 179–94

Dammers J, Schiek M, Boers F, Silex C, Zvyaginstev M, Pletrzyk U and Mathiak K 2008 Integration of amplitude and phase statistics for complete artifact removal in independent components of neuromagnetic recordings *IEEE Trans. Biomed. Eng.* **55** 2353–62

De Lucia M, Fritschy J, Dayan P and Holder D S 2008 A novel method for automated classification of epileptiform activity in the human electroencephalogram-based on independent component analysis *Med. Biol. Eng. Comput.* **46** 263–72

De Martino F, Gentile F, Esposito F, Balsi M, Di Salle F, Goebel R and Formisano E 2007 Classification of fMRI independent components using IC-fingerprints and support vector machine classifiers *NeuroImage* **34** 177–94

Debener S, Hine J, Bleeck S and Eyles J 2008 Source localization of auditory evoked potentials after cochlear implantation *Psychophysiology* **45** 20–4

Debener S, Makeig S, Delorme A and Engel A K 2005 What is novel in the novelty oddball paradigm? Functional significance of the novelty P3 event-related potential as revealed by independent component analysis *Cogn. Brain Res.* **22** 309–21

Debener S, Strobel A, Sorger B, Peters J, Kranczioch C, Engel A K and Goebel R 2007 Improved quality of auditory event-related potentials recorded simultaneously with 3-T fMRI: removal of the ballistocardiogram artefact *NeuroImage* **34** 587–97

Delorme A and Makeig S 2004 EEGLAB: an open source toolbox for analysis of single-trial EEG dynamics including independent component analysis *J. Neurosci. Methods* **134** 9–21

Delorme A, Sejnowski T and Makeig S 2007 Enhanced detection of artifacts in EEG data using higher-order statistics and independent component analysis *NeuroImage* **34** 1443–49
Engdahl B, Leuthold A C, Tan H-R M, Lewis S M, Winskowski A M, Dikel T N and Georgopoulos A P 2010 Post-traumatic stress disorder: a right temporal lobe syndrome? *J. Neural Eng.* **7** 06605
Engell A D and Haxby J V 2007 Facial expression and gaze-direction in human superior temporal sulcus *Neuropsychologia* **45** 3234–41
Escudero J, Hornero R, Abásolo D, Fernández A and López-Coronado M 2007 Artifact removal in magnetoencephalogram background activity with independent component analysis *IEEE Trans. Biomed. Eng.* **54** 1965–73
Fairhall S L and Ishai A 2007 Effective connectivity within the distributed cortical network for face perception *Cereb. Cortex* **17** 2400–6
Fatourechi M, Bashashati A, Ward R K and Birch G E 2007 EMG and EOG artifacts in brain computer interface systems: a survey *Clin. Neurophysiol.* **118** 480–94
Fischl B, Sereno M I and Dale A M 1999 Cortical surface-based analysis: II. Inflation, flattening, and a surface-based coordinate system *NeuroImage* **9** 195–207
Fogelson N, Loukas C, Brown J and Brown P 2004 A common N400 EEG component reflecting contextual integration irrespective of symbolic form *Clin. Neurophysiol.* **115** 1349–58
Fuchs M, Wagner M, Kohler T and Wischmann H A 1999 Linear and nonlinear current density reconstructions *J. Clin. Neurophysiol.* **16** 267–95
Gaetz M, Weinberg H, Rzempoluck E and Jantzen K J 1998 Neural network classifications and correlation analysis of EEG and MEG activity accompanying spontaneous reversals of the Necker cube *Cogn. Brain Res.* **6** 335–46
Georgopoulos A P *et al* 2007 Synchronous neural interactions assessed by magnetoencephalography: a functional biomarker for brain disorders *J. Neural Eng.* **4** 349
Georgopoulos A P, Tan H R M, Lewis S M, Leuthold A C, Winskowski A M, Lynch J K and Engdahl B 2010 The synchronous neural interactions test as a functional neuromarker for post-traumatic stress disorder (PTSD): a robust classification method based on the bootstrap *J. Neural Eng.* **7** 016011
Gevins A S, Doyle J C, Cutillo B A, Schaffer R E, Tannehill R S and Bressler S L 1985 Neurocognitive pattern-analysis of a visuospatial task—rapidly-shifting foci of evoked correlations between electrodes *Psychophysiology* **22** 32–43
Grech R, Cassar T, Muscat J, Camilleri K P, Fabri S G, Zervakis M, Xanthopoulos P, Sakkalis V and Vanrumste B 2008 Review on solving the inverse problem in EEG source analysis *J. Neuroeng. Rehabil.* **5** 25
Groppe D M, Makeig S and Kutas M 2009 Identifying reliable independent components via split-half comparisons *NeuroImage* **45** 1199–211
Gross J, Kujala J, Hämäläinen M, Timmermann L, Schnitzler A and Salmelin R 2001 Dynamic imaging of coherent sources: studying neural interactions in the human brain *Proc. Natl Acad. Sci. USA* **98** 694–99
Hämäläinen M S and Ilmoniemi R J 1994 Interpreting magnetic-fields of the brain—minimum norm estimates *Med. Biol. Eng. Comput.* **32** 35–42
Hauk O 2004 Keep it simple: a case for using classical minimum norm estimation in the analysis of EEG and MEG data *NeuroImage* **21** 1612–21
Haxby J V, Hoffman E A and Gobbini M I 2000 The distributed human neural system for face perception *Trends Cogn. Sci.* **4** 223–33
Haxby J V, Hoffman E A and Gobbini M I 2002 Human neural systems for face recognition and social communication *Biol. Psychiatry* **51** 59–67
Himberg J, Hyvärinen A and Esposito F 2004 Validating the independent components of neuroimaging time series via clustering and visualization *NeuroImage* **22** 1214–22
Hyvärinen A and Oja E 2000 Independent component analysis: algorithms and applications *Neural Netw.* **13** 411–30
Hyvärinen A, Ramkumar P, Parkkonen L and Hari R 2010 Independent component analysis of short-time Fourier transforms for spontaneous EEG/MEG analysis *NeuroImage* **49** 257–71
Ishai A 2008 Let's face it: it's a cortical network *NeuroImage* **40** 415–19
Jervis B, Belal S, Camilleri K, Cassar T, Bigan C, Linden D E J, Michalopoulos K, Zervakis M, Besleaga M and Fabri S 2007 The independent components of auditory P300 and CNV evoked potentials derived from single-trial recordings *Physiol. Meas.* **28** 745–71
Joyce C A, Gorodnitsky I F and Kutas M 2004 Automatic removal of eye movement and blink artifacts from EEG data using blind component separation *Psychophysiology* **41** 313–25
Jung T-P, Makeig S, Humphries C, Lee T-W, McKeown M J, Iragui V and Sejnowski T J 2000 Removing electroencephalographic artifacts by blind source separation *Psychophysiology* **37** 163–78
Jung T-P, Makeig S, Westerfield M, Townsend J, Courchesne E and Sejnowski T J 2001 Analysis and visualization of single-trial event-related potentials *Hum. Brain Mapp.* **14** 166–85
Kachenoura A, Albera L, Senhadji L and Comon P 2008 ICA: a potential tool for BCI systems *IEEE Signal Process. Mag.* **25** 57–68
Kamousi B, Amini A N and He B 2007 Classification of motor imagery by means of cortical current density estimation and Von Neumann entropy *J. Neural Eng.* **4** 17
Klopp J, Marinkovic K, Chauvel P, Nenov V and Halgren E 2000 Early widespread cortical distribution of coherent fusiform face selective activity *Hum. Brain Mapp.* **11** 286–93
Kobayashi K, Akiyama T, Nakahori T, Yoshinaga H and Gotman J 2002 Systematic source estimation of spikes by a combination of independent component analysis and RAP-MUSIC I: principles and simulation study *Clin. Neurophysiol.* **113** 713–24
Latif M A, Sanei S, Chambers J and Spyrou L 2007 Partially constrained blind source separation for localization of unknown sources exploiting non-homogeneity of the head tissues *J. VLSI Signal Process. Syst.* **49** 217–32
Lee P-L, Hsieh J-C, Wu C-H, Shyu K-K, Chen S-S, Yeh T-C and Wu Y-T 2006 The brain computer interface using flash visual evoked potential and independent component analysis *Ann. Biomed. Eng.* **34** 1641–54
Lee P-L, Wu Y-T, Chen L-F, Chen Y-S, Cheng C-M, Yeh T-C, Ho L-T, Chang M-S and Hsieh J-C 2003 ICA-based spatiotemporal approach for single-trial analysis of postmovement MEG beta synchronization *NeuroImage* **20** 2010–30
Lee P-S, Chen Y-S, Hsieh J-C, Su T-P and Chen L-F 2010 Distinct neuronal oscillatory responses between patients with bipolar and unipolar disorders: a magnetoencephalographic study *J. Affect. Disord.* **123** 270–75
Lee T-W, Girolami M and Sejnowski T J 1999 Independent component analysis using an extended infomax algorithm for mixed subGaussian and superGaussian sources *Neural Comput.* **11** 417–41
Lemm S, Curio G, Hlushchuk Y and Muller K R 2006 Enhancing the signal-to-noise ratio of ICA-based extracted ERPs *IEEE Trans. Biomed. Eng.* **53** 601–7
Li Y D, Ma Z W and Lu W K 2006 Automatic removal of the eye blink artifact from EEG using an ICA-based template matching approach *Physiol. Meas.* **27** 425–36

Liu J-X, Chen Y-S and Chen L-F 2010 Fast and accurate registration techniques for affine and nonrigid alignment of MR brain images *Ann. Biomed. Eng.* **38** 138–57
Lou B, Hong B, Gao X R and Gao S K 2008 Bipolar electrode selection for a motor imagery based brain-computer interface *J. Neural Eng.* **5** 342
Lu Y L, Cao P G, Sun J J, Wang J, Li L M, Ren Q S, Chen Y and Chai X Y 2012 Using independent component analysis to remove artifacts in visual cortex responses elicited by electrical stimulation of the optic nerve *J. Neural Eng.* **9** 026002
Makeig S, Debener S, Onton J and Delorme A 2004 Mining event-related brain dynamics *Trends Cogn. Sci.* **8** 204–10
Makeig S, Westerfield M, Jung T-P, Covington J, Townsend J, Sejnowski T J and Courchesne E 1999 Functionally independent components of the late positive event-related potential during visual spatial attention *J. Neurosci.* **19** 2665–80
Mantini D, Franciotti R, Romani G L and Pizzella V 2008 Improving MEG source localizations: an automated method for complete artifact removal based on independent component analysis *NeuroImage* **40** 160–73
Michel C M, Murray M M, Lantz G, Gonzalez S, Spinelli L and de Peralta R G 2004 EEG source imaging *Clin. Neurophysiol.* **115** 2195–222
Milanesi M, James C J, Martini N, Menicucci D, Gemignani A, Ghelarducci B and Landini L 2009 Objective selection of EEG late potentials through residual dependence estimation of independent components *Physiol. Meas.* **30** 779–94
Mosher J C, Leahy R M and Lewis P S 1999 EEG and MEG: forward solutions for inverse methods *IEEE Trans. Biomed. Eng.* **46** 245–59
Naeem M, Brunner C, Leeb R, Graimann B and Pfurtscheller G 2006 Separability of four-class motor imagery data using independent components analysis *J. Neural Eng.* **3** 208–16
Onton J, Delorme A and Makeig S 2005 Frontal midline EEG dynamics during working memory *NeuroImage* **27** 341–56
Ossadtchi A, Baillet S, Mosher J C, Thyerlei D, Sutherling W and Leahy R M 2004 Automated interictal spike detection and source localization in magnetoencephalography using independent components analysis and spatiotemporal clustering *Clin. Neurophysiol.* **115** 508–22
Pascualmarqui R D, Michel C M and Lehmann D 1994 Low resolution electromagnetic tomography—a new method for localizing electrical-activity in the brain *Int. J. Psychophysiol.* **18** 49–65
Pritchard W S, Houlihan M E and Robinson J H 1999 P300 and response selection: a new look using independent-components analysis *Brain Topogr.* **12** 31–7
Roberts S J and Everson R 2000 *Independent Component Analysis: Principles and Practice* (Cambridge: Cambridge University Press) pp 299–314
Rong F and Contreras-Vidal J L 2006 Magnetoencephalographic artifact identification and automatic removal based on independent component analysis and categorization approaches *J. Neurosci. Methods* **157** 337–54
Saatchi R 2004 Single-trial lambda wave identification using a fuzzy inference system and predictive statistical diagnosis *J. Neural Eng.* **1** 21
Said C P, Moore C D, Engell A D, Todorov A and Haxby J V 2010 Distributed representations of dynamic facial expressions in the superior temporal sulcus *J. Vis.* **10** 11
Scherg M and Von Cramon D 1985 Two bilateral sources of the late AEP as identified by a spatio-temporal dipole model *Electroencephalogr. Clin. Neurophysiol.* **62** 32–44
Sekihara K and Nagarajan S S 2008 *Adaptive Spatial Filters for Electromagnetic Brain Imaging* (Berlin: Springer) pp 9–25
Serby H, Yom-Tov E and Inbar G F 2005 An improved P300-based brain-computer interface *IEEE Trans. Neural Syst. Rehabil. Eng.* **13** 89–98
Sercheli M S, Bilevicius E, Alessio A, Ozelo H, Pereira F R S, Rondina J M, Cendes F and Covolan R J M 2009 EEG spike source localization before and after surgery for temporal lobe epilepsy: a BOLD EEG-fMRI and independent component analysis study *Braz. J. Med. Biol. Res.* **42** 582–87
Tang A C, Pearlmutter B A, Malaszenko N A and Phung D B 2002a Independent components of magnetoencephalography: single-trial response onset times *NeuroImage* **17** 1773–89
Tang A C, Pearlmutter B A, Malaszenko N A, Phung D B and Reeb B C 2002b Independent components of magnetoencephalography: localization *Neural Comput.* **14** 1827–58
Tang A C, Sutherland M T and McKinney C J 2005 Validation of SOBI components from high-density EEG *NeuroImage* **25** 539–53
Tikhonov A N and Arsenin V I 1977 *Solutions of Ill-posed Problems* (New York: Wiley)
Tsai A C, Liou M, Jung T-P, Onton J A, Cheng P-E, Huang C-C, Duann J-R and Makeig S 2006 Mapping single-trial EEG records on the cortical surface through a spatiotemporal modality *NeuroImage* **32** 195–207
Turi G, Gotthardt S, Singer W, Vuong T A, Munk M and Wibral M 2012 Quantifying additive evoked contributions to the event-related potential *NeuroImage* **59** 2607–24
Uutela K, Hämäläinen M and Somersalo E 1999 Visualization of magnetoencephalographic data using minimum current estimates *NeuroImage* **10** 173–80
Varela F, Lachaux J-P, Rodriguez E and Martinerie J 2001 The brainweb: phase synchronization and large-scale integration *Nat. Rev. Neurosci.* **2** 229–39
Vigário R, Särelä J, Jousmäki V, Hämäläinen M and Oja E 2000 Independent component approach to the analysis of EEG and MEG recordings *IEEE Trans. Biomed. Eng.* **47** 589–93
Viola F C, Thorne J, Edmonds B, Schneider T, Eichele T and Debener S 2009 Semi-automatic identification of independent components representing EEG artifact *Clin. Neurophysiol.* **120** 868–77
Wessel J R and Ullsperger M 2011 Selection of independent components representing event-related brain potentials: a data-driven approach for greater objectivity *NeuroImage* **54** 2105–15
Xu N, Gao X R, Hong B, Miao X B, Gao S K and Yang F S 2004 BCI competition 2003—data set IIb: enhancing P300 wave detection using ICA-based subspace projections for BCI applications *IEEE Trans. Biomed. Eng.* **51** 1067–72
Zarzoso V and Comon P 2010 Robust independent component analysis by iterative maximization of the kurtosis contrast with algebraic optimal step size *IEEE Trans. Neural Netw.* **21** 248–61
Zhukov L, Weinstein D and Johnson C 2000 Independent component analysis for EEG source localization—an algorithm that reduces the complexity of localizing multiple neural sources *IEEE Eng. Med. Biol. Mag.* **19** 87–96